Three-Dimensional Modeling and Simulation of Wideband MIMO Mobile-to-Mobile Channels

Alenka G. Zajić, *Member, IEEE*, and Gordon L. Stüber, *Fellow, IEEE*

***Abstract*—A three-dimensional (3-D) geometrical propagation model for wideband multiple-input multiple-output (MIMO) mobile-to-mobile (M-to-M) communications is proposed. Based on the geometrical model, a 3-D parametric reference model for wideband MIMO M-to-M multipath fading channels is developed. From the reference model, the corresponding space-time-frequency correlation function is derived for a 3-D non-isotropic scattering environment. It is shown that the time and frequency dispersion of a wide sense stationary uncorrelated scattering channel cannot be treated independently, contrary to common practice. From the space-time-frequency correlation function, the space-Doppler power spectral density and the power space-delay spectrum are derived and compared with measured data. Finally, a new sum-of-sinusoids based simulation model for wideband MIMO M-to-M Ricean fading channels is proposed. The statistics of the simulation model are verified by simulation. The results show that the simulation model is a good approximation of the reference model.**

***Index Terms*—Mobile-to-mobile channels, wideband channels, fading channel simulator, Ricean fading, sum-of-sinusoids.**

I. Introduction

MOBILE ad-hoc wireless networks, intelligent transportation systems, and relay-based cellular networks all use mobile-to-mobile (M-to-M) communication channels. M-to-M communication systems are equipped with low elevation antennas and have both the transmitter $\mathrm{T_x}$ and the receiver $\mathrm{R_x}$ in motion. To successfully design M-to-M systems, it is necessary to have a detailed knowledge of the outdoor multipath fading channel and its statistical properties. Early studies of single-input single-output (SISO) M-to-M Rayleigh fading channels have been reported by Akki and Haber in [1] and [2]. They showed that the received envelope of M-to-M channels is Rayleigh faded under non-line-of-sight (NLoS) conditions, but the statistical properties differ from conventional fixed-to-mobile cellular radio channels. They were the first to propose a two-dimensional (2-D) reference model for single-input single-output (SISO) M-to-M Rayleigh fading channels. Methods for simulating SISO M-to-M channels have been proposed in [3]-[5]. Channel sounding measurements for narrowband and wideband SISO M-to-M channels have been reported in [6]-[8]. The 2-D reference and simulation models for narrowband multiple-input multiple-output (MIMO) M-to-M channels have been proposed in [9]-[12]. All these previously reported 2-D models assume that the field incident on the $\mathrm{T_x}$ or the $\mathrm{R_x}$ antenna is composed of a number of waves travelling only in the *horizontal* plane. This assumption is accurate only for certain environments, e.g., rural areas. This assumption does not seem appropriate for an urban environment where the $\mathrm{T_x}$ and $\mathrm{R_x}$ antenna arrays are often located in close proximity to and lower than surrounding buildings and other objects. To overcome these shortcomings, we have recently proposed a three-dimensional (3-D) reference model for *narrowband* MIMO M-to-M multipath fading channels [14]. However, to completely characterize MIMO M-to-M multipath fading channels, it is necessary to develop 3-D models for *wideband* MIMO M-to-M channels.

This paper introduces new 3-D reference and simulation models for *wideband* MIMO M-to-M channels and shows that these models can match the measured data in a variety of urban environments, which is a lacking feature of previously reported 2-D and 3-D M-to-M models. Here, we consider MIMO communication links between vehicles travelling on urban surface street (USS) and Interstate highway (IH) road surfaces. The previously reported 2-D and 3-D models do not always match the SISO measurements for vehicles travelling in a convoy fashion [6]-[8], especially for IH environments. One possible reason for this mismatch is the presence of single-bounced rays, which are ignored in the previously proposed models (i.e., only double-bounced rays are considered). Note that the single-bounced rays, if present, bear more energy than the double-bounced rays, and cannot be ignored. In this paper, we propose a 3-D mathematical reference model for wideband MIMO M-to-M channels that accounts for line-of-sight (LoS), single-bounced at the transmit side (SBT), single-bounced at the receive side (SBR), and double-bounced (DB) rays.

To describe our 3-D reference model, we first introduce a 3-D geometrical model for wideband MIMO M-to-M channels, called the concentric-cylinders model. This model is extension of the two-cylinder model for narrowband M-to-M channels proposed in [14]. Then, we propose a parametric reference model that employs the concentric-cylinders geometry and constructs the input delay-spread function as a superposition of LoS, SBT, SBR, and DB rays. The parametric nature of the model makes it adaptable to a variety of propagation environ-

Manuscript received April 9, 2007; revised June 23, 2008; accepted December 10, 2008. The associate editor coordinating the review of this paper and approving it for publication was K. Sowerby.

This work was prepared through collaborative participation in the Collaborative Technology Alliance for Communications & Networks sponsored by the U.S. Army Research Laboratory under Cooperative Agreement DAAD19-01-2-0011. The U.S. Government is authorized to reproduce and distribute reprints for Government purposes notwithstanding any copyright notation thereon. The views and conclusions contained in this document are those of the authors and should not be interpreted as representing the official policies, either expressed or implied, of the Army Research Laboratory or the U. S. Government.

A. G. Zajić was with the School of Electrical and Computer Engineering, Georgia Institute of Technology, Atlanta, GA 30332 USA. She is now with AlZaComm, Atlanta GA 30328.

Gordon L. Stüber is with the School of Electrical and Computer Engineering, Georgia Institute of Technology, Atlanta, GA 30332 USA (e-mail: stuber@ece.gatech.edu).

Digital Object Identifier 10.1109/TWC.2009.070379

ments, i.e., USS and IH environments. From the new reference model, we derive the corresponding space-time-frequency correlation function (STF-CF) for a 3-D non-isotropic scattering environment and show that the time and frequency dispersion of a wide sense stationary uncorrelated scattering (WSSUS) channel cannot be treated independently. Furthermore, we derive the space-Doppler power spectral density (sD-psd) and the power space-delay spectrum (psds) for the same scattering environment. Finally, we compare the SISO sD-psd and psds with those obtained from SISO measurements in [6]-[8] to illustrate the importance of combining the LoS, SBT, SBR and DB rays.

To fully validate our 3-D reference model, we need to compare the first- and second-order statistics of the proposed models with those obtained from the MIMO measurements. Since the only measurements available in the open literature were for the SISO systems, we have conducted a MIMO M-to-M channel-sounding experimental campaign along surface streets and on the Interstate highways in the Midtown Atlanta metropolitan area. Details of the experimental equipment and methodology, the method to process the data, the method to extract model parameters from the measured data, and the validation of the proposed 3-D reference model in terms of the cumulative distribution functions (CDF), STF-CF, sD-psd, psds, and level crossing rates (LCR) are presented in [15]. Second-order statistics, such as LCR and average fade duration are non-trivial and are the subject of our work in [16]. In contrast, this paper focuses on the detailed derivations of the STF-CF, sD-psd and psds, and shows that the statistical correlation functions are largely influenced by the relative power mixture of DB, SBT, SBR, and LoS ray components.

This paper goes further to present a sum-of-sinusoids based (SoS) simulation model. Since our reference model assumes an infinite number of scatterers at the $\mathrm{T_x}$ and the $\mathrm{R_x}$, which prevents practical implementation, we propose a SoS based simulation model for a 3-D non-isotropic scattering environment that consists of a finite number of scatterers at the $\mathrm{T_x}$ and the $\mathrm{R_x}$. We employ a concentric-cylinders model that combines LoS, SBT, SBR, and DB rays and where the in-phase (I) and the quadrature (Q) components of the time-variant transfer function are orthogonal functions. The statistical properties of our simulation model are verified by comparison with the corresponding statistical properties of the reference model. The results show that the simulation model is a good approximation of the reference model.

The remainder of the paper is organized as follows. Section II introduces the geometrical concentric-cylinders model and presents a 3-D reference model for wideband MIMO M-to-M channels. Section III derives the STF-CF, the sD-psd, and the psds for a 3-D non-isotropic scattering environment. Section IV details the SoS simulation model. Finally, Section V provides some concluding remarks.

II. A Reference Model for Wideband MIMO M-to-M Channels

This paper considers a wideband MIMO communication link between vehicles travelling on USS and IH road surfaces. It is assumed that both the $\mathrm{T_x}$ and the $\mathrm{R_x}$ are in motion and equipped with L_t transmit and L_r receive low elevated omnidirectional antenna elements. The radio propagation in outdoor metropolitan environments is characterized by 3-D WSSUS with either LoS or NLoS conditions between the $\mathrm{T_x}$ and the $\mathrm{R_x}$. The MIMO channel can be described by an $L_r \times L_t$ matrix $\mathbf{H}(t,\tau) = [h_{ij}(t,\tau)]_{L_r \times L_t}$ of the input delay-spread functions.

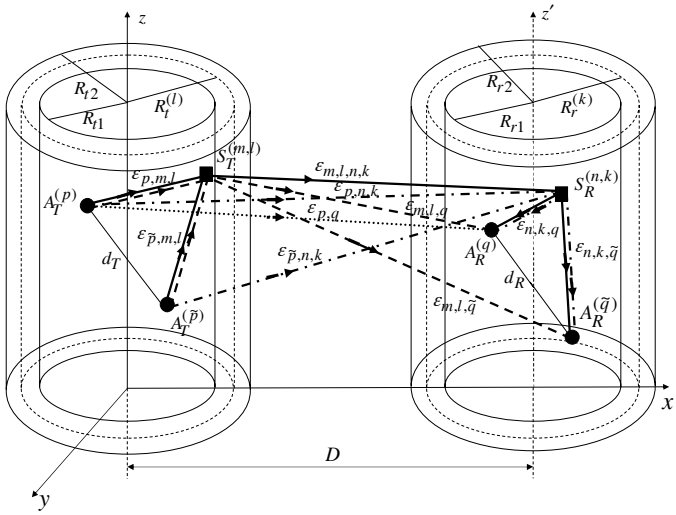

Fig. 1. The concentric-cylinders model with LoS , SBT, SBR, and DB rays for a MIMO M-to-M channel with $L_t = L_r = 2$ antenna elements.

Fig. 1 shows the concentric-cylinders model with LoS, SBT, SBR, and DB rays for a MIMO M-to-M channel with $L_t = L_r = 2$ antenna elements. Vertical concentric cylinders are chosen to model the scattering surfaces and diffracting edges because most of the structures in outdoor metropolitan environments (e.g., buildings, highway dividers, etc.) have straight vertical surfaces. The elementary 2×2 antenna configuration in Fig. 1 will be used later to construct uniform linear antenna arrays with an arbitrary number of omnidirectional antenna elements. The concentric-cylinders model defines four vertical cylinders, two around the $\mathrm{T_x}$ and another two around the $\mathrm{R_x}$, as shown in Fig. 1. Around the transmitter, M fixed omnidirectional scatterers occupy the volume between cylinders of radii R_{t1} and R_{t2}. It is assumed that the M scatterers lie on L cylindric surfaces of radii $R_{t1} \leq R_t^{(l)} \leq R_{t2}$, where $1 \leq l \leq L$. The lth cylindric surface contains $M^{(l)}$ fixed omnidirectional scatterers, and the (m,l)th transmit scatterer is denoted by $S_T^{(m,l)}$, where $1 \leq m \leq M^{(l)}$. Similarly, around the receiver, N fixed omnidirectional scatterers occupy a volume between cylinders of radii R_{r1} and R_{r2}. It is assumed that the N scatterers lie on F cylindric surfaces of radii $R_{r1} \leq R_r^{(k)} \leq R_{r2}$, where $1 \leq k \leq F$. The kth cylindric surface contains $N^{(k)}$ fixed omnidirectional scatterers, and the (n,k)th receive scatterer is denoted by $S_R^{(n,k)}$, where $1 \leq n \leq N^{(k)}$. The distance between the centers of the $\mathrm{T_x}$ and $\mathrm{R_x}$ cylinders is D. It is assumed that the radii R_{t2} and R_{r2} are sufficiently smaller than the distance D (local scattering condition). Furthermore, it is assumed that the distance D is smaller than $4R_{t1}R_{r1}L_r/(\lambda(L_t-1)(L_r-1))$ so that the channel does not experience keyhole behavior [17], where λ denotes the carrier wavelength. The spacing between antenna

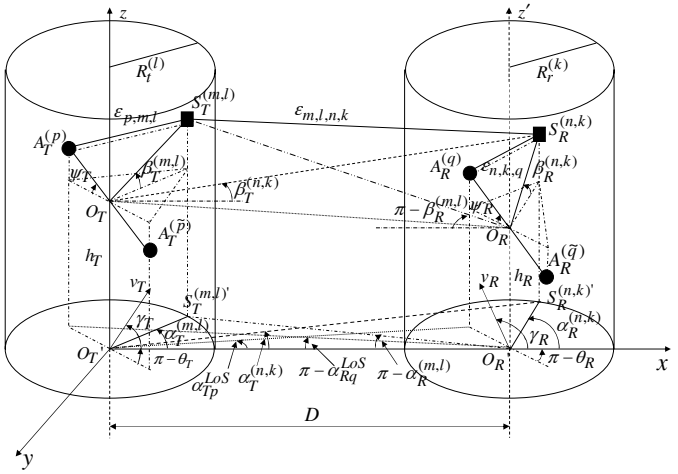

Fig. 2. The lth and kth cylinders from Fig. 1 with the detailed geometry of the LoS , SBT, SBR, and DB rays.

elements at the $\mathrm{T_x}$ and the $\mathrm{R_x}$ is denoted by d_T and d_R, respectively. It is assumed that d_T and d_R are much smaller than the radii R_{t1} and R_{r1}. The symbols $\epsilon_{p,m,l}$, $\epsilon_{m,l,q}$, $\epsilon_{p,n,k}$, $\epsilon_{n,k,q}$, $\epsilon_{m,l,n,k}$, and $\epsilon_{p,q}$ denote distances $A_T^{(p)}$–$S_T^{(m,l)}$, $S_T^{(m,l)}$–$A_R^{(q)}$, $A_T^{(p)}$–$S_R^{(n,k)}$, $S_R^{(n,k)}$–$A_R^{(q)}$, $S_T^{(m,l)}$–$S_R^{(n,k)}$, and $A_T^{(p)}$–$A_R^{(q)}$ respectively, as shown in Fig. 1. For ease of reference, Fig. 2 shows only one of the L cylindric surfaces around the $\mathrm{T_x}$ and one of F cylindric surfaces around the $\mathrm{R_x}$ and details the geometry of the LoS , SBT, SBR, and DB rays. Angles θ_T and θ_R in Fig. 2 describe the orientation of the $\mathrm{T_x}$ and $\mathrm{R_x}$ antenna array in the x–y plane, respectively, relative to the x-axis. Similarly, angles ψ_T and ψ_R describe the elevation of the $\mathrm{T_x}$'s antenna array and the $\mathrm{R_x}$'s antenna array relative to the x–y plane, respectively. The $\mathrm{T_x}$ and $\mathrm{R_x}$ are moving with speeds v_T and v_R in directions described by angles γ_T and γ_R in the x–y plane (relative to the x-axis), respectively. The symbols $\alpha_T^{(m,l)}$ and $\alpha_T^{(n,k)}$ are the azimuth angles of departures (AAoD) of the waves that impinge on the scatterers $S_T^{(m,l)}$ and $S_R^{(n,k)}$, respectively, whereas $\alpha_R^{(m,l)}$ and $\alpha_R^{(n,k)}$ are the azimuth angles of arrivals (AAoA) of the waves scattered from $S_T^{(m,l)}$ and $S_R^{(n,k)}$, respectively. Similarly, the symbols $\beta_T^{(m,l)}$ and $\beta_R^{(n,k)}$ denote the elevation angle of departure (EAoD) and the elevation angle of arrival (EAoA), respectively. Finally, the symbols α_{Rq}^{LoS}, α_{Tp}^{LoS} denote the AAoDs and AAoAs of the LoS paths. For ease of reference, the parameters defined in Figs. 1 and 2 are summarized in Table I.

Observe from the 3-D geometrical model in Fig. 1 that some waves from the $\mathrm{T_x}$ antenna elements may traverse directly to the $\mathrm{R_x}$ antenna elements (LoS rays) , while others are single-bounced at the $\mathrm{T_x}$ (i.e., the waves from the $\mathrm{T_x}$ antenna elements scatter from the scatterers located around the $\mathrm{T_x}$ before arriving at the $\mathrm{R_x}$ antenna elements), single-bounced at the $\mathrm{R_x}$ (i.e., the waves from the $\mathrm{T_x}$ antenna elements scatter from the scatterers located around the $\mathrm{R_x}$ before arriving at the $\mathrm{R_x}$ antenna elements), and/or double-bounced (i.e., the waves from the $\mathrm{T_x}$ antenna elements impinge on the scatterers located around the $\mathrm{T_x}$ and scatter from the scatterers located around the $\mathrm{R_x}$ before arriving at the $\mathrm{R_x}$ antenna elements). Hence, the input delay-spread function of the link $A_T^{(p)}$ - $A_R^{(q)}$

TABLE I
DEFINITION OF THE PARAMETERS USED IN THE CONCENTRIC-CYLINDERS GEOMETRICAL MODEL.

D	The distance between the centers of the Tx and Rx cylinders.
$R_t^{(l)}, R_r^{(k)}$	The radius of the l^{th} Tx and k^{th} Rx cylinder, respectively.
d_T, d_R	The spacing between two adjacent antenna elements at the Tx and Rx, respectively.
θ_T, θ_R	The orientation of the Tx and Rx antenna array in the x-y plane (relative to the x-axis), respectively.
ψ_T, ψ_R	The elevation of the Tx's and Rx's antenna array relative to the x-y plane, respectively.
v_T, v_R	The velocities of the Tx and Rx, respectively.
γ_T, γ_R	The moving directions of the Tx and Rx, in the x-y plane (relative to the x-axis), respectively.
h_T, h_R	The distances $d\left(O_T, O_T^{'}\right)$ and $d\left(O_R, O_R^{'}\right)$, respectively.
R_{t1}, R_{t2}, R_{r1}, R_{r2}	The min and max radii of the cylinders around the Tx and Rx, respectively.
$\alpha_T^{(m,l)}, \alpha_T^{(n,k)}$	The azimuth angles of departure (AAoD) of the waves that impinge on the scatterers $S_T^{(m,l)}$ and $S_R^{(n,k)}$, respectively.
$\alpha_R^{(m,l)}, \alpha_R^{(n,k)}$	The azimuth angles of arrival (AAoA) of the waves scattered from $S_T^{(m,l)}$ and $S_R^{(n,k)}$, respectively.
$\beta_T^{(m,l)}, \beta_T^{(n,k)}$	The elevation angles of departure (EAoD) of the waves that impinge on the scatterers $S_T^{(m,l)}$ and $S_R^{(n,k)}$, respectively.
$\beta_R^{(m,l)}, \beta_R^{(n,k)}$	The elevation angles of arrival (EAoA) of the waves scattered from $S_T^{(m,l)}$ and $S_R^{(n,k)}$, respectively.
α_{Rq}^{LoS}, α_{Tp}^{LoS}	The AAoA and the AAoD of the LoS paths, respectively.
$\varepsilon_{p,m,l}$, $\varepsilon_{m,l,q}$, $\varepsilon_{p,n,k}$, $\varepsilon_{n,k,q}$, $\varepsilon_{m,l,n,k}$ and ε_{pq}	The distances $d\left(A_T^{(p)}, S_T^{(m,l)}\right)$, $d\left(S_T^{(m,l)}, A_R^{(q)}\right)$, $d\left(A_T^{(p)}, S_R^{(n,k)}\right)$, $d\left(S_T^{(m)}, S_R^{(n)}\right)$, $d\left(S_R^{(n,k)}, A_R^{(q)}\right)$, $d\left(S_T^{(m,l)}, S_R^{(n,k)}\right)$, and $d\left(A_T^{(p)}, A_R^{(q)}\right)$, respectively.

can be written as a superposition of the LoS, SBT, SBR, and DB rays, viz.

$$h_{pq}(t,\tau) = h_{pq}^{SBT}(t,\tau) + h_{pq}^{SBR}(t,\tau) + h_{pq}^{DB}(t,\tau) + h_{pq}^{LoS}(t,\tau). \tag{1}$$

The single-bounced components of the input delay-spread function are, respectively,

$$h_{pq}^{SBT}(t,\tau) = \sqrt{\frac{\eta_T}{K+1}} \lim_{M\to\infty} \frac{1}{\sqrt{M}} \sum_{l=1}^{L} \sum_{m=1}^{M^{(l)}} \xi_{m,l} g_{m,l}(t) \times \delta(\tau - \tau_{m,l}) \sqrt{G_p\left(\alpha_T^{(m,l)}, \beta_T^{(m,l)}\right) G_q\left(\alpha_R^{(m,l)}, \beta_R^{(m,l)}\right)}, \tag{2}$$

$$h_{pq}^{SBR}(t,\tau) = \sqrt{\frac{\eta_R}{K+1}} \lim_{N\to\infty} \frac{1}{\sqrt{N}} \sum_{k=1}^{F} \sum_{n=1}^{N^{(k)}} \xi_{n,k} g_{n,k}(t) \times \delta(\tau - \tau_{n,k}) \sqrt{G_p\left(\alpha_T^{(n,k)}, \beta_T^{(n,k)}\right) G_q\left(\alpha_R^{(n,k)}, \beta_R^{(n,k)}\right)}, \tag{3}$$

where $G_p(\cdot,\cdot)$ and $G_q(\cdot,\cdot)$ denote the antenna patterns of the pth transmit and qth receive antenna element, respectively. Furthermore, $\xi_{m,l}$, $\xi_{n,k}$, denote the amplitudes and $\tau_{m,l}$, and $\tau_{n,k}$ denote the time delays of the multipath components. Finally, functions $g_{m,l}(t)$ and $g_{n,k}(t)$ are defined as

$$g_{m,l}(t) = e^{-j\frac{2\pi}{\lambda}(\epsilon_{p,m,l}+\epsilon_{m,l,q})+j\phi_{m,l}} \tag{4}$$
$$e^{j2\pi t\left[f_{T\max}\cos(\alpha_T^{(m,l)}-\gamma_T)\cos\beta_T^{(m,l)}+f_{R\max}\cos(\alpha_R^{(m,l)}-\gamma_R)\cos\beta_R^{(m,l)}\right]},$$

$$g_{n,k}(t) = e^{-j\frac{2\pi}{\lambda}(\epsilon_{p,n,k}+\epsilon_{n,k,q})+j\phi_{n,k}} \tag{5}$$
$$e^{j2\pi t\left[f_{T\max}\cos(\alpha_T^{(n,k)}-\gamma_T)\cos\beta_T^{(n,k)}+f_{R\max}\cos(\alpha_R^{(n,k)}-\gamma_R)\cos\beta_R^{(n,k)}\right]},$$

where $f_{T\max} = v_T/\lambda$ and $f_{R\max} = v_R/\lambda$ are the maximum Doppler frequencies associated with the $\mathrm{T_x}$ and $\mathrm{R_x}$, respectively. The amplitudes of the multipath components, $\xi_{m,l}$ and $\xi_{n,k}$, are defined as

$$\xi_{m,l} = \frac{\sqrt{P_{pq}}\lambda}{4\pi}\left[\left|d\left(O_T, S^{(m,l)}\right)\right| + \left|d\left(S^{(m,l)}, O_R\right)\right|\right]^{-\gamma/2} \approx \Omega_{pq}\left(1 - \frac{\gamma}{2}\frac{R_t^{(l)}}{D}\right), \quad (6)$$

$$\xi_{n,k} = \frac{\sqrt{P_{pq}}\lambda}{4\pi}\left[\left|d\left(O_T, S^{(n,k)}\right)\right| + \left|d\left(S^{(n,k)}, O_R\right)\right|\right]^{-\gamma/2} \approx \Omega_{pq}\left(1 - \frac{\gamma}{2}\frac{R_r^{(k)}}{D}\right), \quad (7)$$

respectively, where P_{pq} is the power transmitted through the subchannel $A_T^{(p)}$–$A_R^{(q)}$, K is the Rice factor (ratio of LoS to scatter received power), γ is the path loss exponent, $d(\cdot,\cdot)$ denotes distance between two points, and $\Omega_{pq} = D^{-\gamma/2}\sqrt{P_{pq}}\lambda/4\pi$. Finally, the time delays $\tau_{m,l}$ and $\tau_{n,k}$ are the travel times of the waves scattered from the scatterers $S_T^{(m,l)}$ and $S_R^{(n,k)}$, i.e.,

$$\tau_{m,l} = \frac{D + R_t^{(l)}(1 - \cos\alpha_T^{(m,l)})}{c_0 \cos\beta_T^{(m,l)}}, \quad (8)$$

$$\tau_{n,k} = \frac{D + R_r^{(k)}(1 + \cos\alpha_R^{(n,k)})}{c_0 \cos\beta_R^{(n,k)}}, \quad (9)$$

where c_0 is the speed of light. The double-bounced component of the input delay-spread function is

$$h_{pq}(t,\tau) = \sqrt{\frac{\eta_{TR}}{K+1}} \lim_{M,N\to\infty} \frac{1}{\sqrt{MN}} \sum_{l,m=1}^{L,M^{(l)}} \sum_{k,n=1}^{F,N^{(k)}} g_{m,l,n,k}(t) \quad (10)$$

$$\xi_{m,l,n,k}\delta(\tau - \tau_{m,l,n,k})\sqrt{G_p(\alpha_T^{(m,l)}, \beta_T^{(m,l)})G_q(\alpha_R^{(n,k)}, \beta_R^{(n,k)})},$$

where $\xi_{m,l,n,k}$ and $\tau_{m,l,n,k}$ denote the amplitudes and time delays of the multipath components, respectively. Function $g_{m,l,n,k}(t)$ is defined as

$$g_{m,l,n,k}(t) = e^{-j\frac{2\pi}{\lambda}(\epsilon_{p,m,l} + \epsilon_{m,l,n,k} + \epsilon_{n,k,q}) + j\phi_{m,l,n,k}} \quad (11)$$
$$e^{j2\pi t\left[f_{T\max}\cos(\alpha_T^{(m,l)} - \gamma_T)\cos\beta_T^{(m,l)} + f_{R\max}\cos(\alpha_R^{(n,k)} - \gamma_R)\cos\beta_R^{(n,k)}\right]}.$$

The amplitude of the multipath component, $\xi_{m,l,n,k}$, is defined as

$$\xi_{m,l,n,k} = \frac{\sqrt{P_{pq}}\lambda}{4\pi}\left[\left|d\left(O_T', S^{(m,l)}\right)\right| + \left|d\left(S^{(m,l)}, S^{(n,k)}\right)\right| + \left|d\left(S^{(n,k)}, O_R'\right)\right|\right]^{\gamma/2} \approx \Omega_{pq}\left(1 - \frac{\gamma}{2}\frac{R_t^{(l)} + R_r^{(k)}}{2D}\right). \quad (12)$$

Finally, the time delay $\tau_{m,l,n,k}$ is the travel time of the wave impinged on the scatterer $S_T^{(m,l)}$ and scattered from the scatterer $S_R^{(n,k)}$, i.e.,

$$\tau_{m,l,n,k} = \frac{D}{c_0} + \frac{R_t^{(l)}(1 - \cos\alpha_T^{(m,l)})}{c_0\cos\beta_T^{(m,l)}} + \frac{R_r^{(k)}(1 + \cos\alpha_R^{(n,k)})}{c_0\cos\beta_R^{(n,k)}}. \quad (13)$$

The parameters η_T, η_R, and η_{TR} in (2), (3), and (10), respectively, specify how much the single- and double-bounced rays contribute in the total power P_{pq}, i.e., these parameters satisfy $\eta_T + \eta_R + \eta_{TR} = 1$. It is assumed that the angles of departure ($\alpha_T^{(m,l)}$, $\alpha_T^{(n,k)}$, $\beta_T^{(m,l)}$, and $\beta_T^{(n,k)}$) and the angles of arrival ($\alpha_R^{(n,k)}$, $\alpha_R^{(m,l)}$, $\beta_R^{(n,k)}$, and $\beta_R^{(m,l)}$) are random variables. Furthermore, it is assumed that the radii $R_t^{(l)}$ and $R_r^{(k)}$ are independent random variables. Finally, it is assumed that the phases $\phi_{m,l}$, $\phi_{n,k}$, and $\phi_{m,l,n,k}$ are uniform random variables on the interval $[-\pi, \pi)$ that are independent from the angles of departure, the angles of arrival, and the radii of the cylinders. Using the assumptions introduced above and the Central Limit Theorem, we can conclude that $h_{pq}^{SBT}(t,\tau)$, $h_{pq}^{SBR}(t,\tau)$, and $h_{pq}^{DB}(t,\tau)$ are independent zero-mean complex Gaussian random processes. Furthermore, note that double-bounced rays have the angles of departure ($\alpha_T^{(m,l)}$ and $\beta_T^{(m,l)}$) independent from the angles of arrival ($\alpha_R^{(n,k)}$ and $\beta_R^{(n,k)}$) [17]. On the other hand, single-bounced rays have angles of arrival ($\alpha_R^{(m,l)}$ and $\beta_R^{(m,l)}$) that are dependent on the angles of departure ($\alpha_T^{(m,l)}$ and $\beta_T^{(m,l)}$) and angles of departure ($\alpha_T^{(n,k)}$ and $\beta_T^{(n,k)}$) that are dependent on the angles of arrival ($\alpha_R^{(n,k)}$ and $\beta_R^{(n,k)}$). Appendix A shows that $\alpha_R^{(m,l)} \approx \pi - \Delta_T^{(l)}\sin\alpha_T^{(m,l)}$, $\beta_R^{(m,l)} \approx \pi - \left(\Delta_T^{(l)}\beta_T^{(m,l)} + \Delta_H/D\right)$, $\alpha_T^{(n,k)} \approx \Delta_R^{(k)}\sin\alpha_R^{(n,k)}$, and $\beta_T^{(n,k)} \approx \Delta_R^{(k)}\beta_R^{(n,k)} - \Delta_H/D$, where $\Delta_T^{(l)} = R_t^{(l)}/D$, $\Delta_R^{(k)} = R_r^{(k)}/D$, and $\Delta_H = h_T - h_R$.

The LoS component of the input delay-spread function is

$$h_{pq}^{LoS}(t,\tau) = \sqrt{\frac{K}{K+1}}\xi_{LoS}g_{LoS}(t)\delta(\tau - \tau_{LoS}) \times \sqrt{G_p\left(\alpha_{Tp}^{LoS}, \beta_{Tp}^{LoS}\right)G_q\left(\alpha_{Rq}^{LoS}, \beta_{Rq}^{LoS}\right)}, \quad (14)$$

where the LoS amplitude is $\xi_{LoS} \approx \Omega_{pq}$, $g^{LoS}(t) = e^{j2\pi t f_{T\max}\cos(\alpha_{Tp}^{LoS} - \gamma_T)}e^{j2\pi t f_{R\max}\cos(\alpha_{Rq}^{LoS} - \gamma_R)}e^{-j\frac{2\pi}{\lambda}\epsilon_{p,q}}$, and the LoS time delay is $\tau_{LoS} = \sqrt{D^2 + \Delta_H^2}/c_0$.

The distances $\epsilon_{m,l,q}$, $\epsilon_{p,n,k}$, $\epsilon_{p,m,l}$, $\epsilon_{n,k,q}$, $\epsilon_{m,l,n,k}$, and $\epsilon_{p,q}$ can be expressed as functions of the random variables $\alpha_T^{(m,l)}$, $\beta_T^{(m,l)}$, $\alpha_R^{(n,k)}$, $\beta_R^{(n,k)}$, α_{Rq}^{LoS}, $R_t^{(l)}$, and $R_r^{(k)}$ as follows:

$$\epsilon_{m,l,q} \approx D - \frac{L_r + 1 - 2q}{2}d_R\cos\psi_R \times \left[\Delta_T^{(l)}\sin\theta_R\sin\alpha_T^{(m,l)} - \cos\theta_R\right], \quad (15)$$

$$\epsilon_{p,n,k} \approx D - \frac{L_t + 1 - 2p}{2}d_T\cos\psi_T \times \left[\Delta_R^{(k)}\sin\theta_T\sin\alpha_R^{(n,k)} + \cos\theta_T\right], \quad (16)$$

$$\epsilon_{p,m,l} \approx R_t^{(l)} - \frac{L_t + 1 - 2p}{2}\left[d_{Tx}\cos\alpha_T^{(m,l)}\cos\beta_T^{(m,l)} + d_{Ty}\sin\alpha_T^{(m,l)}\cos\beta_T^{(m,l)} + d_{Tz}\sin\beta_T^{(m,l)}\right], \quad (17)$$

$$\epsilon_{n,k,q} \approx R_r^{(k)} - \frac{L_r + 1 - 2q}{2}\left[d_{Rx}\cos\alpha_R^{(n,k)}\cos\beta_R^{(n,k)} + d_{Ry}\sin\alpha_R^{(n,k)}\cos\beta_R^{(n,k)} + d_{Rz}\sin\beta_R^{(n,k)}\right], \quad (18)$$

$$\epsilon_{m,l,n,k} \approx D, \quad (19)$$

$$\epsilon_{p,q} \approx D - 0.5(L_t + 1 - 2p)d_T\cos\psi_T\cos\theta_T - 0.5 \times (L_r + 1 - 2q)d_R\cos\psi_R\cos(\alpha_{Rq}^{LoS} - \theta_R), \quad (20)$$

where parameters p and q take values from the sets $p \in$

$\{1,\ldots,L_t\}$ and $q \in \{1,\ldots,L_r\}$, respectively, $d_{Tx} = d_T\cos\psi_T\cos\theta_T$, $d_{Ty} = d_T\cos\psi_T\sin\theta_T$, $d_{Tz} = d_T\sin\psi_T$, $d_{Rx} = d_R\cos\psi_R\cos\theta_R$, $d_{Ry} = d_R\cos\psi_R\sin\theta_R$, $d_{Rz} = d_R\sin\psi_R$. The approximations in (15)–(20) are due to small angle approximations ($\sin x \approx x$, $\cos x \approx 1$ for small x), while the derivations are omitted for brevity.

To simplify further analysis, we use the time-variant transfer function instead of the input delay-spread function and we normalize the gain patterns of the antenna elements to unity (i.e., we assume omnidirectional antennas), although other gain patterns can be accommodated at this point. The time-variant transfer function is the Fourier transform of the input delay-spread function [18] and can be written as

$$\begin{aligned} T_{pq}(t,f) &= \mathcal{F}_\tau\{h_{pq}(t,\tau)\} = T_{pq}^{SBT}(t,f) + T_{pq}^{SBR}(t,f) \\ &+ T_{pq}^{DB}(t,f) + T_{pq}^{LoS}(t,f), \end{aligned} \quad (21)$$

where $T_{pq}^{SBT}(t,f)$ is the SBT, $T_{pq}^{SBR}(t,f)$ is the SBR, $T_{pq}^{DB}(t,f)$ is the DB, and $T_{pq}^{LoS}(t,f)$ is the LoS component of the time-variant transfer function. The expressions for $T_{pq}^{SBT}(t,f)$, $T_{pq}^{SBR}(t,f)$, $T_{pq}^{DB}(t,f)$, and $T_{pq}^{LoS}(t,f)$ are derived in Appendix B.

Several different scatterer distributions, such as uniform, Gaussian, Laplacian, and von Mises, are used in prior work to characterize the azimuth angles of departure $\alpha_T^{(m,l)}$ and arrival $\alpha_R^{(n,k)}$. We use the von Mises probability density function (pdf) because it approximates many of the previously mentioned distributions and admits closed-form solutions for many useful situations. The von Mises pdf is defined as [19]

$$f(\theta) = \exp\left[\kappa\cos(\theta-\mu)\right]/2\pi I_0(\kappa), \quad (22)$$

where $\theta \in [-\pi,\pi)$, $I_0(\cdot)$ is the zeroth-order modified Bessel function of the first kind, $\mu \in [-\pi,\pi)$ is the mean angle at which the scatterers are distributed in the x–y plane, and κ controls the spread of scatterers around the mean. When $\kappa = 0$, $f(\theta) = 1/(2\pi)$ is a uniform distribution yielding isotropic scattering in the horizontal plane. As κ increases, the scatterers become more clustered around mean angle μ and the scattering becomes increasingly non-isotropic. Prior work uses several different scatterer distributions, such as uniform, cosine, and Gaussian, to characterize the random elevation angles of departure and arrival, $\beta_T^{(m,l)}$ and $\beta_R^{(n,k)}$. We use the pdf [20]

$$f(\varphi) = \begin{cases} \frac{\pi}{4|\varphi_m|}\cos\left(\frac{\pi}{2}\frac{\varphi}{\varphi_m}\right) & , \ |\varphi| \le |\varphi_m| \le \frac{\pi}{2} \\ 0 & , \ \text{otherwise} \end{cases} \quad (23)$$

where φ_m is the maximum elevation angle and lies in the range $0^\circ \le |\varphi_m| \le 20^\circ$ [21]. Such maximum elevation angles are typical for the "street-canyon" type of propagation, which is prevalent in M-to-M communications where both the $\mathrm{T_x}$ and $\mathrm{R_x}$ are in motion and equipped with low elevation antennas (e.g., two vehicles driving along streets). Finally, the radii $R_t^{(l)}$ and $R_r^{(k)}$ are characterized using the pdf $f(R) = 2R/(R_2^2 - R_1^2)$. Such a distribution implies that the scatterers in the horizontal plane will have a uniform density between the cylinders R_{t1} and R_{t2} at the transmitter and cylinders R_{r1} and R_{r2} at the receiver, if the scattering is isotropic in the horizontal plane.

III. Space-Time-Frequency Correlation Function, Space-Doppler Power Spectrum, and Power Delay Spectrum of the 3-D Reference Model

Assuming a 3-D non-isotropic scattering environment, we first derive the STF-CF of the 3-D reference model and show that the time and frequency dispersion of the WSSUS channel cannot be treated independently. From the STF-CF we derive the corresponding sD-psd and psds. Finally, we present some analytical results for the sD-psd and psds and compare them with measured data.

A. STF-CF

The normalized STF-CF between two time-variant transfer functions defined in (21), i.e., $T_{pq}(t,f)$ and $T_{\tilde{p}\tilde{q}}(t,f)$, is defined as

$$R_{pq,\tilde{p}\tilde{q}}(\Delta t,\Delta f) = \frac{\mathrm{E}\left[T_{pq}(t,f)^* T_{\tilde{p}\tilde{q}}(t+\Delta t, f+\Delta f)\right]}{\sqrt{\mathrm{Var}[T_{pq}(t,f)]\mathrm{Var}[T_{\tilde{p}\tilde{q}}(t,f)]}}, \quad (24)$$

where $(\cdot)^*$ denotes complex conjugate operation, $\mathrm{E}[\cdot]$ is the statistical expectation operator, $\mathrm{Var}[\cdot]$ is the statistical variance operator, $p,\tilde{p} \in \{1,\ldots,L_t\}$, $q,\tilde{q} \in \{1,\ldots,L_r\}$. Since $T_{pq}^{SBT}(t,f)$, $T_{pq}^{SBR}(t,f)$, and $T_{pq}^{DB}(t,f)$ are independent zero-mean complex Gaussian random processes, (24) can be simplified to

$$\begin{aligned} R_{pq,\tilde{p}\tilde{q}}(\Delta t,\Delta f) &= R_{pq,\tilde{p}\tilde{q}}^{SBT}(\Delta t,\Delta f) + R_{pq,\tilde{p}\tilde{q}}^{SBR}(\Delta t,\Delta f) \\ &+ R_{pq,\tilde{p}\tilde{q}}^{DB}(\Delta t,\Delta f) + R_{pq,\tilde{p}\tilde{q}}^{LoS}(\Delta t,\Delta f), \end{aligned} \quad (25)$$

where $R_{pq,\tilde{p}\tilde{q}}^{SBT}(\Delta t,\Delta f)$, $R_{pq,\tilde{p}\tilde{q}}^{SBR}(\Delta t,\Delta f)$, $R_{pq,\tilde{p}\tilde{q}}^{DB}(\Delta t,\Delta f)$, and $R_{pq,\tilde{p}\tilde{q}}^{LoS}(\Delta t,\Delta f)$ denote the normalized STF-CFs of the SBT, SBR, DB, and LoS components, respectively, and are defined as

$$R_{pq,\tilde{p}\tilde{q}}^{SBT}(\Delta t,\Delta f) = \frac{\mathrm{E}\left[T_{pq}^{SBT}(t,f)^* T_{\tilde{p}\tilde{q}}^{SBT}(t+\Delta t,f+\Delta f)\right]}{\Omega_{pq}/(1+K)}, \quad (26)$$

$$R_{pq,\tilde{p}\tilde{q}}^{SBR}(\Delta t,\Delta f) = \frac{\mathrm{E}\left[T_{pq}^{SBR}(t,f)^* T_{\tilde{p}\tilde{q}}^{SBR}(t+\Delta t,f+\Delta f)\right]}{\Omega_{pq}/(1+K)}, \quad (27)$$

$$R_{pq,\tilde{p}\tilde{q}}^{DB}(\Delta t,\Delta f) = \frac{\mathrm{E}\left[T_{pq}^{DB}(t,f)^* T_{\tilde{p}\tilde{q}}^{DB}(t+\Delta t,f+\Delta f)\right]}{\Omega_{pq}/(1+K)}, \quad (28)$$

$$R_{pq,\tilde{p}\tilde{q}}^{LoS}(\Delta t,\Delta f) = \frac{\mathrm{E}\left[T_{pq}^{LoS}(t,f)^* T_{\tilde{p}\tilde{q}}^{LoS}(t+\Delta t,f+\Delta f)\right]}{\Omega_{pq}/(K+1)}. \quad (29)$$

Since the number of local scatterers in the reference model described in Section II is infinite, the discrete AAoDs, $\alpha_T^{(m,l)}$, EAoDs, $\beta_T^{(m,l)}$, AAoAs, $\alpha_R^{(n,k)}$, EAoAs, $\beta_R^{(n,k)}$, and radii $R_t^{(l)}$ and $R_r^{(k)}$ can be replaced with continuous random variables α_T, β_T, α_R, β_R, R_t, and R_r with probability density functions (pdf) $f(\alpha_T)$, $f(\beta_T)$, $f(\alpha_R)$, $f(\beta_R)$, $f(R_t)$, and $f(R_r)$, respectively. To characterize the $\mathrm{T_x}$ and $\mathrm{R_x}$ azimuth angles, we use the von Mises pdf in (22) and denote these pdfs as $f(\alpha_T) = \exp\left[k_T\cos(\alpha_T-\mu_T)\right]/2\pi I_0(k_T)$ and $f(\alpha_R) = \exp\left[k_R\cos(\alpha_R-\mu_R)\right]/2\pi I_0(k_R)$, respectively. To characterize the $\mathrm{T_x}$ and $\mathrm{R_x}$ elevation angles, we use the pdf in (23) and denote these pdfs as $f(\beta_T) = \pi\cos(\pi\beta_T/(2\beta_{T_m}))/(4|\beta_{T_m}|)$,

and $f(\beta_R) = \pi\cos(\pi\beta_R/(2\beta_{R_m}))/(4|\beta_{R_m}|)$, respectively. Finally, to characterize the radii R_t and R_r we use the pdfs $f(R_t) = 2R_t/(R_{t2}^2 - R_{t1}^2)$ and $f(R_r) = 2R_r/(R_{r2}^2 - R_{r1}^2)$, respectively. Using trigonometric transformations, the equality $\int_{-\pi}^{\pi}\exp\{a\sin(c) + b\cos(c)\}dc = 2\pi I_0\left(\sqrt{a^2+b^2}\right)$ [13, eq. 3.338-4], and the results in [14], the STF-CFs of the SBT, SBR, and DB components can be closely approximated as

$$R_{pq,\tilde{p}\tilde{q}}^{SBT}(\Delta t,\Delta f) \approx \frac{\eta_T}{I_0(k_T)}\frac{\cos\left(\frac{2\pi}{\lambda}\beta_{Tm}(p-\tilde{p})d_{Tz}\right)}{1-\left(\frac{4\beta_{Tm}(p-\tilde{p})d_{Tz}}{\lambda}\right)^2} \tag{30}$$
$$\times\, e^{-j\frac{2\pi}{\lambda}(q-\tilde{q})d_{Rx}-j2\pi\Delta t f_{R\max}\cos\gamma_R}\int_{R_{t1}}^{R_{t2}}\left(1-\gamma\frac{R_t}{D}\right)$$
$$\times\, e^{-j\frac{2\pi}{c_0}\Delta f(D+R_t)}I_0\left(\sqrt{x_{SBT}^2+y_{SBT}^2}\right)\frac{2R_t}{R_{t2}^2-R_{t1}^2}dR_t,$$
$$R_{pq,\tilde{p}\tilde{q}}^{SBR}(\Delta t,\Delta f) \approx \frac{\eta_R}{I_0(k_R)}\frac{\cos\left(\frac{2\pi}{\lambda}\beta_{Rm}(q-\tilde{q})d_{Rz}\right)}{1-\left(\frac{4\beta_{Rm}(q-\tilde{q})d_{Rz}}{\lambda}\right)^2} \tag{31}$$
$$\times\, e^{j\frac{2\pi}{\lambda}(p-\tilde{p})d_{Tx}+j2\pi\Delta t f_{T\max}\cos\gamma_T}\int_{R_{r1}}^{R_{r2}}\left(1-\gamma\frac{R_r}{D}\right)$$
$$\times\, e^{-j\frac{2\pi}{c_0}\Delta f(D+R_r)}I_0\left(\sqrt{x_{SBR}^2+y_{SBR}^2}\right)\frac{2R_r}{R_{r2}^2-R_{r1}^2}dR_r,$$
$$R_{pq,\tilde{p}\tilde{q}}^{DB}(\Delta t,\Delta f) \approx \int_{R_{t1}}^{R_{t2}}2e^{-j\frac{2\pi}{c_0}\Delta f R_t}R_t I_0\left(\sqrt{x_{DB}^2+y_{DB}^2}\right)dR_t$$
$$\times A_{DB}\int_{R_{r1}}^{R_{r2}}e^{-j\frac{2\pi}{c_0}\Delta f R_r}R_r I_0\left(\sqrt{w_{DB}^2+z_{DB}^2}\right)\left(1-\gamma\frac{R_r}{D}\right)dR_r$$
$$+A_{DB}\int_{R_{r1}}^{R_{r2}}2e^{-j\frac{2\pi}{c_0}\Delta f R_r}R_r I_0\left(\sqrt{w_{DB}^2+z_{DB}^2}\right)dR_r$$
$$\times\int_{R_{t1}}^{R_{t2}}e^{-j\frac{2\pi}{c_0}\Delta f R_t}R_t I_0\left(\sqrt{x_{DB}^2+y_{DB}^2}\right)\left(1-\gamma\frac{R_t}{D}\right)dR_t, \tag{32}$$

where parameters x_{SBT}, y_{SBT}, x_{SBR}, y_{SBR}, x_{DB}, y_{DB}, z_{DB}, w_{DB}, and A_{DB} are

$$x_{SBT} \approx j(2\pi/\lambda)(p-\tilde{p})d_{Tx} + j2\pi\Delta t f_{T\max}\cos\gamma_T + j2\pi\Delta f R_t/c_0 + k_T\cos\mu_T \tag{33}$$
$$y_{SBT} \approx j2\pi(p-\tilde{p})d_{Ty}/\lambda + j2\pi(q-\tilde{q})d_{Ry}\Delta_T/\lambda + j2\pi\Delta t\left(f_{T\max}\sin\gamma_T + f_{R\max}\Delta_T\sin\gamma_R\right) + k_T\sin\mu_T \tag{34}$$
$$x_{SBR} \approx j(2\pi/\lambda)(q-\tilde{q})d_{Rx} + j2\pi\Delta t f_{R\max}\cos\gamma_R - j2\pi\Delta f R_r/c_0 + k_R\cos\mu_R \tag{35}$$
$$y_{SBR} \approx j2\pi\big[(q-\tilde{q})d_{Ry}/\lambda + (p-\tilde{p})d_{Ty}\Delta_R/\lambda + \Delta t\left(f_{R\max}\sin\gamma_R + f_{T\max}\Delta_R\sin\gamma_T\right)\big] + k_R\sin\mu_R \tag{36}$$
$$x_{DB} \approx j(2\pi/\lambda)(p-\tilde{p})d_{Tx} + j2\pi\Delta t f_{T\max}\cos\gamma_T + j2\pi\Delta f R_t/c_0 + k_T\cos\mu_T \tag{37}$$
$$y_{DB} \approx j(2\pi/\lambda)(p-\tilde{p})d_{Ty} + j2\pi\Delta t f_{T\max}\sin\gamma_T + k_T\sin\mu_T \tag{38}$$
$$z_{DB} \approx j(2\pi/\lambda)(q-\tilde{q})d_{Rx} + j2\pi\Delta t f_{R\max}\cos\gamma_R - j2\pi\Delta f R_r/c_0 + k_R\cos\mu_R \tag{39}$$
$$w_{DB} \approx j(2\pi/\lambda)(q-\tilde{q})d_{Ry} + j2\pi\Delta t f_{R\max}\sin\gamma_R + k_R\sin\mu_R \tag{40}$$
$$A_{DB} = \frac{\eta_{TR}}{I_0(k_T)I_0(k_R)}\frac{\cos\left(\frac{2\pi}{\lambda}\beta_{Tm}(p-\tilde{p})d_{Tz}\right)}{1-\left(\frac{4\beta_{Tm}(p-\tilde{p})d_{Tz}}{\lambda}\right)^2} \tag{41}$$
$$\times\,\frac{\cos\left(\frac{2\pi}{\lambda}\beta_{Rm}(q-\tilde{q})d_{Rz}\right)}{1-\left(\frac{4\beta_{Rm}(q-\tilde{q})d_{Rz}}{\lambda}\right)^2}\frac{e^{-j2\pi\Delta f D/c_0}}{(R_{t2}^2-R_{t1}^2)(R_{r2}^2-R_{r1}^2)}.$$

Using (76), (29) and the approximation $\alpha_{Rq}^{LoS} = \alpha_{R\tilde{q}}^{LoS} \approx \pi$, the STF-CF of the LoS component can be approximated as

$$R_{pq,\tilde{p}\tilde{q}}^{LoS}(\Delta t,\Delta f) \approx Ke^{j\frac{2\pi}{\lambda}[(p-\tilde{p})d_{Tx}-(q-\tilde{q})d_{Rx}]} \times\, e^{j2\pi\Delta t[f_{T\max}\cos\gamma_T - f_{R\max}\cos\gamma_R]-\frac{2\pi}{c_0}\Delta f\sqrt{D^2+\Delta_H{}^2}}. \tag{42}$$

Note that the STF-CFs for the SBT, SBR, and DB components of the time-variant transfer function must be evaluated numerically because the integrals in (30)–(32) do not have closed-form solutions. However, if we assume that the time and frequency dispersion are statistically independent, closed-form expressions for the STF-CFs of the SBT, SBR, and DB components can be obtained. In the literature, it is often assumed that the time dispersion (i.e., the time delays) and the frequency dispersion (i.e., the Doppler spreads) are statistically independent because the time delays depend on the relative locations of the random scatterers (i.e., the angles of arrival, the angles of departure, and the distances among the $\mathrm{T_x}$, $\mathrm{R_x}$, and scatterers), whereas the Doppler spreads depend on the motions of the $\mathrm{T_x}$ and $\mathrm{R_x}$ [22], [23]. However, the Doppler spread depends not only on the speeds of the $\mathrm{T_x}$ and $\mathrm{R_x}$, but also on the angles of departure and the angles of arrival. Hence, both the time delays and the Doppler spreads depend on the relative location of the random scatterers, which implies that they are not statistically independent. Since the angles of departure and the angels of arrival cannot be neglected in the Doppler spreads, another way to obtain the independence between the time delays and the Doppler spreads is to assume that the waves scattered form the relatively closely spaced scatterers have equal time delays. Then, the influence of the angles of arrival and the angles of departure on the time delays can be neglected, making the time delays and the Doppler spreads statistically independent. The 2-D geometry-based statistical models often achieve the independence between the time delays and the Doppler spreads, assuming that all waves scattered from the scatterers lying on the same circle have equal time delays [18]. These time delays are equal to the average of all time delays obtained from the scatterers lying on the same circle. The equivalent assumption in our 3-D concentric cylinders model is that all waves scattered from the scatterers lying on the same cylindric surface have equal (averaged) time delays. Using this approach, the time delays in (8), (9), and (13) can be approximated as

$$\tau_{m,l} \approx \tau_l = (D + R_t^{(l)})/c_0 \tag{43}$$

$$\tau_{n,k} \approx \tau_k = (D + R_r^{(k)})/c_0, \tag{44}$$
$$\tau_{m,l,n,k} \approx \tau_{l,k} = (D + R_t^{(l)} + R_r^{(k)})/c_0. \tag{45}$$

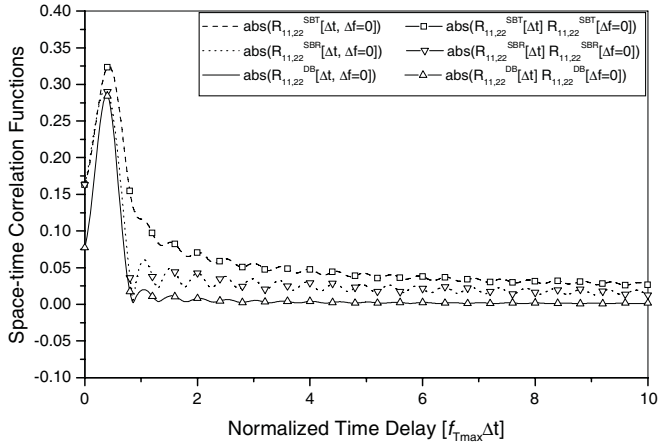

Fig. 3. Comparison of the normalized space-time correlation functions in (30)–(32) and (83)–(85).

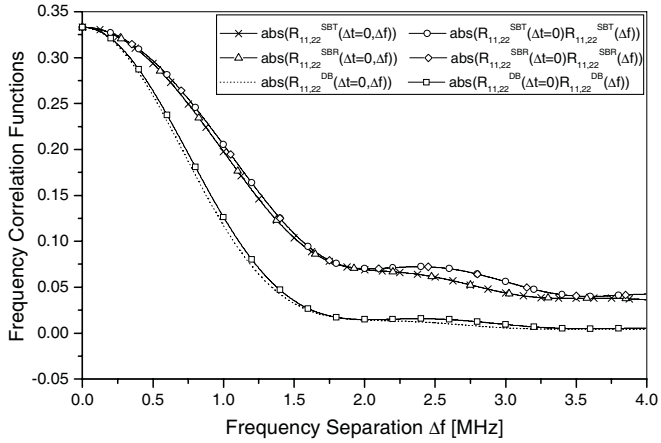

Fig. 4. Comparison of the frequency correlation functions in (30)–(32) and (83)–(85).

Under these assumptions, the space-time-frequency correlation function in (25) can be factored as [23]

$$\begin{aligned} &R_{pq,\tilde{p}\tilde{q}}(\Delta t, \Delta f) = \\ &= R^{SBT}_{pq,\tilde{p}\tilde{q}}(\Delta t) R^{SBT}_{pq,\tilde{p}\tilde{q}}(\Delta f) + R^{SBR}_{pq,\tilde{p}\tilde{q}}(\Delta t) R^{SBR}_{pq,\tilde{p}\tilde{q}}(\Delta f) \\ &+ R^{DB}_{pq,\tilde{p}\tilde{q}}(\Delta t) R^{DB}_{pq,\tilde{p}\tilde{q}}(\Delta f) + R^{LoS}_{pq,\tilde{p}\tilde{q}}(\Delta t) R^{LoS}_{pq,\tilde{p}\tilde{q}}(\Delta f), \quad (46) \end{aligned}$$

where the closed-form expressions for correlations $R^{SBT}_{pq,\tilde{p}\tilde{q}}(\Delta t)$, $R^{SBT}_{pq,\tilde{p}\tilde{q}}(\Delta f)$, $R^{SBR}_{pq,\tilde{p}\tilde{q}}(\Delta t)$, $R^{SBR}_{pq,\tilde{p}\tilde{q}}(\Delta f)$, $R^{DB}_{pq,\tilde{p}\tilde{q}}(\Delta t)$, and $R^{DB}_{pq,\tilde{p}\tilde{q}}(\Delta f)$ are derived in Appendix C, while the closed-form space-time-frequency correlation function of the LoS component, i.e., $R^{LoS}_{pq,\tilde{p}\tilde{q}}(\Delta t) R^{LoS}_{pq,\tilde{p}\tilde{q}}(\Delta f)$, remains the same as in (42).

To validate assumptions used to obtain the closed-form space-time-frequency correlation functions in (83)–(85), we compare these equations with the numerically obtained space-time-frequency correlations in (30)–(32). Figs. 3–5 compare the space-time correlation functions, the frequency correlation functions, and the space-time-frequency correlation functions in (30)–(32) and (83)–(85). The parameters used to obtain curves in Figs. 3–5 are summarized in Columns III–V of Table II. Fig. 3 shows excellent agreement between the space-time correlation functions. This is an expected result, because the approximations in (43)–(45) affect only time delays, which

TABLE II
PARAMETERS USED IN FIGS. 3–10.

Parameters	Definition	Fig.3	Fig.4	Fig.5	Fig.6	Fig.7	Fig.8	Fig.9	Fig. 10
D [m]	The distance between the Tx and Rx.	500	500	500	300	300	300	300	200
d_T d_R	The spacing between two adjacent antenna elements at the Tx and Rx, respectively.	0.5λ 0.5λ	0 0	0.5λ 0.5λ	$0,1\lambda$ $0,1\lambda$	$0,1\lambda$ $0,1\lambda$	$0\text{-}4\lambda$ $0\text{-}4\lambda$	$0\text{-}4\lambda$ $0\text{-}4\lambda$	0.5λ 0.5λ
θ_T θ_R	The orientation of the Tx and Rx antenna array in the x-y plane (relative to the x-axis), respectively.	$\frac{\pi}{4}$ $\frac{\pi}{4}$	$\frac{\pi}{4}$ $\frac{\pi}{4}$	$\frac{\pi}{4}$ $\frac{\pi}{4}$	0° 0°	90° 90°	0° 0°	0° 0°	$\frac{\pi}{4}$ $\frac{\pi}{4}$
ψ_T ψ_R	The elevation of the Tx's and Rx's antenna array relative to the x-y plane, respectively.	$\frac{\pi}{6}$ $\frac{\pi}{6}$	$\frac{\pi}{6}$ $\frac{\pi}{6}$	$\frac{\pi}{6}$ $\frac{\pi}{6}$	0° 0°	0° 0°	0° 0°	0° 0°	$\frac{\pi}{3}$ $\frac{\pi}{3}$
γ_T γ_R	The moving directions of the Tx and Rx, in the x-y plane (relative to the x-axis), respectively.	40° 20°	40° 20°	40° 20°	90° 90°	0° 0°	90° 90°	90° 90°	20° 20°
Δ_H [m]	The difference between the Tx and Rx antenna heights.	0	0	0	0	0	0	0	0
λ [m]	The wavelength	0.3	0.3	0.3	0.058	0.123	0.123	0.123	0.3
$f_{T\max}$ [Hz] $f_{R\max}$ [Hz]	The maximum Doppler frequencies.	200 200	200 200	200 200	75 75	200 200	200 200	200 200	200 200
γ	The path loss exponent	4	4	4	4	4	4	4	4
K	The Rice factor	0	0	0	4	1.5	0	0	2
k_T k_R	The spread of scatterers around the mean; the parameter in the von Mises pdf.	2 2	2 2	2 2	5 3.3	4 4	9.1 9.1	9.4 9.4	1 1
μ_T μ_R	The mean angle at which the scatterers are distributed in the x-y plane; the parameter in the von Mises pdf.	$\frac{\pi}{2}$ $\frac{3\pi}{2}$	$\frac{\pi}{2}$ $\frac{3\pi}{2}$	$\frac{\pi}{2}$ $\frac{3\pi}{2}$	70° 250°	0° 180°	$\frac{\pi}{2}$ $\frac{3\pi}{2}$	$\frac{\pi}{2}$ $\frac{3\pi}{2}$	0 π
β_{Tm} β_{Rm}	The maximum elevation angles.	15° 15°	15° 15°	15° 15°	20° 20°	15° 15°	15° 15°	15° 15°	15° 15°
R_{t1} [m] R_{t2} [m] R_{r1} [m] R_{r2} [m]	The min and max radii of the cylinders around the Tx and Rx, respectively.	10 100 10 100	10 100 10 100	10 100 10 100	9 90 9 90	9.6 96 9.6 96	13 130 13 130	12 120 12 120	4 40 4 40
η_T η_R η_{TR}	Specify how much the single- and double-bounced rays contribute in the total averaged power, i.e., $\eta_T+\eta_R+\eta_{TR}=1$	$\frac{1}{3}$ $\frac{1}{3}$ $\frac{1}{3}$	$\frac{1}{3}$ $\frac{1}{3}$ $\frac{1}{3}$	$\frac{1}{3}$ $\frac{1}{3}$ $\frac{1}{3}$	0.1 0.1 0.8	0.3 0.3 0.4	0.2 0.2 0.6	0.45 0.45 0.1	Defined in the text

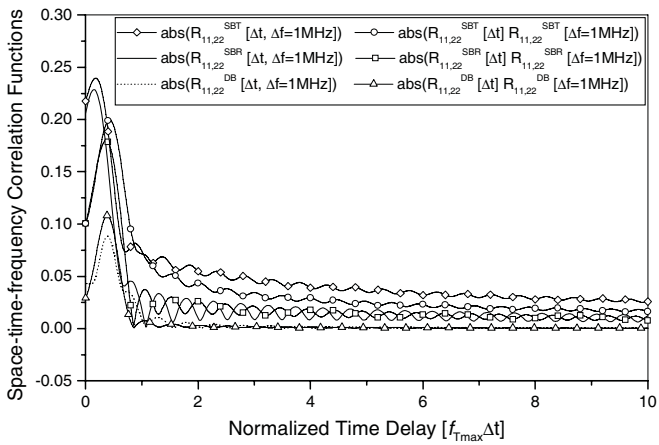

Fig. 5. Comparison of the normalized space-time-frequency correlation functions in (30)–(32) and (83)–(85).

are set to zero in both the closed-form and numerically obtained space-time correlation functions. Fig. 4 shows relatively good agreement between the frequency correlation functions. Note that the frequency correlation functions are obtained from the space-time-frequency correlation functions by eliminating the space and time components (i.e., by setting $d_T = d_R = \Delta t = 0$). Hence, this result shows that the approximated and exact time delays have similar values, i.e.,

verifies the approximations in (43)–(45). However, Fig. 5 shows that equations (83)–(85) underestimate the space-time-frequency correlation functions. This discrepancy is due to the fact that the time delays in the closed-form expressions are not functions of the angles of departure or the angles of arrival and do not affect the Bessel functions in (83)–(85). On the other hand, the time delays in the numerically obtained expressions are functions of the angles of departure and the angles of arrival and affect the Bessel functions in (30)–(32). Even small differences between the input values of the Bessel functions in (30)–(32) and (83)–(85), respectively, can significantly change the final results. Hence, the influence of the angles of arrival and the angles of departure on the time delays cannot be neglected and the numerically obtained space-time-frequency correlation functions in (30)–(32) should be used. Note that similar results are obtained for the 2-D models (i.e., for $\beta_{Tm} = \beta_{Rm} = 0°$). These results are not surprising because in the practice, the time delays and the Doppler spreads are not independent [24].

B. sD-psd

The sD-psd of the time-variant transfer function is the Fourier transform of the space-time correlation function $R_{pq,\tilde{p}\tilde{q}}(\Delta t, \Delta f = 0)$. From (25), it follows that the sD-psd is a summation of the sD-psd functions of the SBT, SBR, DB, and LoS components. Appendix D shows that the sD-psds of the LoS, SBT, SBR and DB components are, respectively,

$$S^{LoS}_{pq,\tilde{p}\tilde{q}}(\nu) = \mathcal{F}_{\Delta t}\{R^{LoS}_{pq,\tilde{p}\tilde{q}}(\Delta t, \Delta f = 0)\} = K e^{j\frac{2\pi}{\lambda}(p-\tilde{p})d_{Tx}} e^{-j\frac{2\pi}{\lambda}(q-\tilde{q})d_{Rx}} \delta(\nu + f_{T\max}\cos\gamma_T - f_{R\max}\cos\gamma_R), \quad (47)$$

$$S^{SBT}_{pq,\tilde{p}\tilde{q}}(\nu) = \mathcal{F}_{\Delta t}\{R^{SBT}_{pq,\tilde{p}\tilde{q}}(\Delta t, \Delta f = 0)\} \quad (48)$$
$$= \frac{\eta_T}{I_0(k_T)} \frac{\cos\left(\frac{2\pi}{\lambda}\beta_{T_m}(p-\tilde{p})d_{Tz}\right)}{1 - \left(\frac{4\beta_{T_m}(p-\tilde{p})d_{Tz}}{\lambda}\right)^2} \times \frac{(3 - 2\gamma R_{t2}/D)R^2_{t2} - (3 - 2\gamma R_{t1}/D)R^2_{t1}}{3(R^2_{t2} - R^2_{t1})} \times \frac{\exp\{j2\pi(\nu + f_{R\max}\cos\gamma_R)A_{SBT} - j2\pi p_{x_{SBR}}\}}{\pi f_{T\max}\sqrt{1 - [(\nu + f_{R\max}\cos\gamma_R)/f_{T\max}]^2}} \times \cosh\Big[(k_T\sin(\mu_T - \gamma_T) + j2\pi p_{x_{SBT}}q_{y_{SBT}} - j2\pi p_{y_{SBT}}q_{x_{SBT}})\sqrt{1 - [(\nu + f_{R\max}\cos\gamma_R)/f_{T\max}]^2}\Big],$$

$$S^{SBR}_{pq,\tilde{p}\tilde{q}}(\nu) = \mathcal{F}_{\Delta t}\{R^{SBR}_{pq,\tilde{p}\tilde{q}}(\Delta t, \Delta f = 0)\} \quad (49)$$
$$= \frac{\eta_R}{I_0(k_R)} \frac{\cos\left(\frac{2\pi}{\lambda}\beta_{R_m}(q-\tilde{q})d_{Rz}\right)}{1 - \left(\frac{4\beta_{R_m}(q-\tilde{q})d_{Rz}}{\lambda}\right)^2} \times \frac{\exp\{j2\pi(\nu - f_{T\max}\cos\gamma_T)A_{SBR} + j2\pi p_{x_{SBT}}\}}{\pi f_{R\max}\sqrt{1 - [(\nu - f_{T\max}\cos\gamma_T)/f_{R\max}]^2}} \times \frac{(3 - 2\gamma R_{r2}/D)R^2_{r2} - (3 - 2\gamma R_{r1}/D)R^2_{r1}}{3(R^2_{r2} - R^2_{r1})} \times \cosh\Big[(k_R\sin(\mu_R - \gamma_R) + j2\pi p_{x_{SBR}}q_{y_{SBR}} - j2\pi p_{y_{SBR}}q_{x_{SBR}})\sqrt{1 - [(\nu - f_{T\max}\cos\gamma_T)/f_{R\max}]^2}\Big],$$

$$S^{DB}_{pq,\tilde{p}\tilde{q}}(\nu) = \mathcal{F}_{\Delta t}\{R^{DB}_{pq,\tilde{p}\tilde{q}}(\Delta t, \Delta f = 0)\} = \frac{\eta_{TR} I_{DB}}{I_0(k_T)I_0(k_R)} \times \frac{\cos\left(\frac{2\pi}{\lambda}\beta_{T_m}(p-\tilde{p})d_{Tz}\right)}{1 - \left(\frac{4\beta_{T_m}(p-\tilde{p})d_{Tz}}{\lambda}\right)^2} \frac{\cos\left(\frac{2\pi}{\lambda}\beta_{R_m}(q-\tilde{q})d_{Rz}\right)}{1 - \left(\frac{4\beta_{R_m}(q-\tilde{q})d_{Rz}}{\lambda}\right)^2} \quad (50)$$
$$\times e^{j(2\pi p_{x_{DB}}q_{x_{DB}} + 2\pi p_{y_{DB}}q_{y_{DB}} - jk_T\cos(\mu_T - \gamma_T))\nu/f_{T\max}} \times \frac{1}{\pi f_{T\max}\sqrt{1 - (\nu/f_{T\max})^2}} \cosh\Big[(k_T\sin(\mu_T - \gamma_T) + j2\pi p_{x_{DB}}q_{y_{DB}} - j2\pi p_{y_{DB}}q_{x_{DB}})\sqrt{1 - (\nu/f_{T\max})^2}\Big] \odot e^{j(2\pi p_{z_{DB}}q_{z_{DB}} + 2\pi p_{w_{DB}}q_{w_{DB}} - jk_R\cos(\mu_R - \gamma_R))\nu/f_{R\max}} \times \frac{1}{\pi f_{R\max}\sqrt{1 - (\nu/f_{R\max})^2}} \cosh\Big[(k_R\sin(\mu_R - \gamma_R) + j2\pi p_{z_{DB}}q_{w_{DB}} - j2\pi p_{w_{DB}}q_{z_{DB}})\sqrt{1 - (\nu/f_{R\max})^2}\Big],$$

where $\mathcal{F}\{\cdot\}$ denotes the Fourier transform, $\cosh(\cdot)$ is the hyperbolic cosine, $\delta(\cdot)$ is the Dirac delta function, $\odot$ denotes convolution, $|\nu + f_{R\max}\cos\gamma_R| \leq f_{T\max}$ and $|\nu - f_{T\max}\cos\gamma_T| \leq f_{R\max}$ for the single-bounced sD-psds, and $|\nu| \leq f_{T\max} + f_{R\max}$ for the double-bounced sD-psd. Finally, the parameters in (48) and (49) are defined in (89), the parameters in (50) are defined in (93), and $I_{DB} = (R^2_{t2} - R^2_{t1})(0.5R^2_{r2} - \gamma R^3_{r2}/(3D) - 0.5R^2_{r1} + \gamma R^3_{r1}/(3D)) + (R^2_{r2} - R^2_{r1})(0.5R^2_{t2} - \gamma R^3_{t2}/(3D) - 0.5R^2_{t1} + \gamma R^3_{t1}/(3D))$.

Fig. 6 plots several SISO and MIMO sD-psds, assuming 3-D non-isotropic scattering and the LoS conditions between the $\mathrm{T_x}$ and $\mathrm{R_x}$. These sD-psds are typical of USS environments. First, we compare our analytical SISO sD-psd with the measured SISO sD-psd in Fig. 8 (a) of [6]. The measurements in [6] were performed in the USS area, at 5.2 GHz, and the maximum Doppler frequencies were $f_{T\max} = f_{R\max} = 75$ Hz. Both, the $\mathrm{T_x}$ and $\mathrm{R_x}$ were equipped with one omnidirectional antenna. The distance between the $\mathrm{T_x}$ and $\mathrm{R_x}$ was approximately $D = 300$ m. The moving directions were $\gamma_T = \gamma_R = 90°$, the antenna orientations were $\theta_T = \theta_R = \psi_T = \psi_R = 0°$, $\Delta_H = 0$. The same parameters are used to obtain all analytical results in Fig. 6. The rest of the parameters in the reference model, i.e., $K = 4$, $\mu_T = 70°$, $k_T = 5$, $\beta_{T_m} = 20°$, $R_{t1} = R_{r1} = 9$ m, $R_{t2} = R_{r2} = 90$ m, $\mu_R = 250°$, $k_R = 3.3$, $\beta_{R_m} = 20°$, $\eta_T = \eta_R = 0.1$, and $\eta_{TR} = 0.8$, are manually estimated to fit the SISO sD-psd reported in [6], and summarized in Column VI of Table II. This approach was necessary since we did not have access to the actual channel measurement data used in [6]. A detailed discussion on how to jointly estimate these parameters from channel measurement data, if available, is presented in [15]. In any case, Fig. 6 shows the close agreement between the theoretical and empirical SISO sD-psds. Furthermore, we note that the M-to-M sD-psd in an urban area differs from the U-shaped sD-psd of cellular channels. This is because the DB rays are more dominant than the SBT and SBR rays (i.e., $\eta_T = \eta_R = 0.1$, and $\eta_{TR} = 0.8$) in an USS area, whereas cellular channels have only SBR and LoS rays (i.e, $\eta_T = 0$, $\eta_R = 1$, $\eta_{TR} = 0$). To illustrate the importance of combining the DB, SBT, and SBR rays, Fig. 6 also plots the SISO sD-

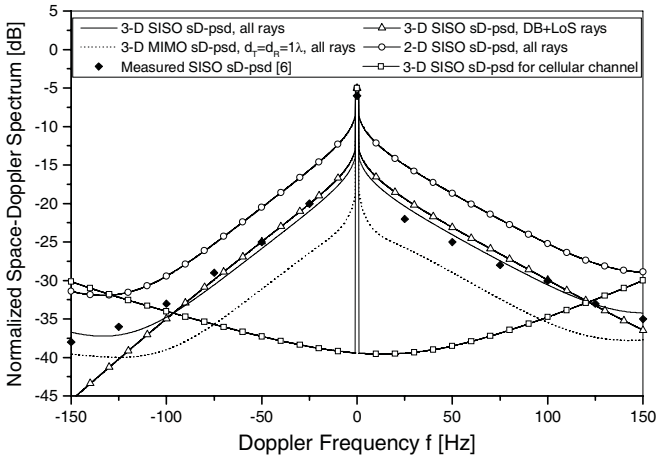

Fig. 6. The normalized theoretical and measured sD-psd in an USS environment.

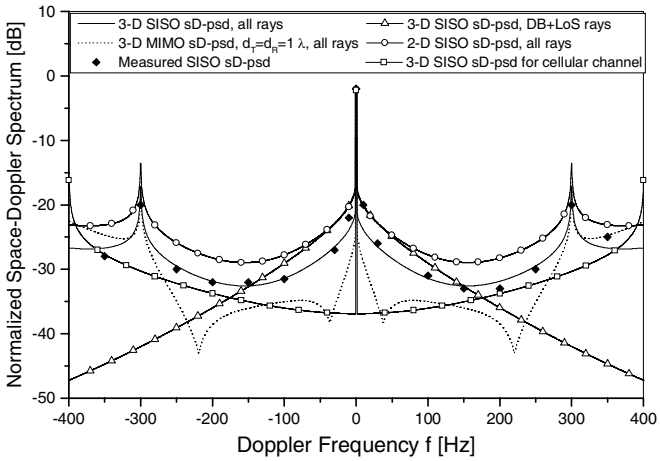

Fig. 7. The normalized theoretical and measured sD-psd in an IH environment.

psd with only DB and LoS rays. The results show that for higher frequencies, the model with only DB and LoS rays overestimates the sD-psd. Furthermore, Fig. 6 shows that the 2-D model (i.e, $\beta_{T_m} = \beta_{R_m} = 0°$) underestimates the sD-psd. Finally, Fig. 6 plots the MIMO sD-psd, $S_{11,22}(\nu)$, with $d_T = d_R = 1\lambda$. The results show that the sD-psd decreases with increased antenna element separation.

Fig. 7 plots several SISO and MIMO sD-psds that can be found in the IH environments. First, we compare our analytical SISO sD-psd with the measured SISO sD-psd in Fig. 4(d) of [7]. The measurements in [7] were performed on the highway, at 2.4 GHz, and the maximum Doppler frequencies were $f_{T\max} = f_{R\max} = 200$ Hz. The vehicles were driven in the rightmost lane and very close to the sound blockers on the edge of the highway. Both, the $\mathrm{T_x}$ and $\mathrm{R_x}$ were equipped with one omnidirectional antenna. The distance between the $\mathrm{T_x}$ and $\mathrm{R_x}$ was approximately $D = 300$ m. The moving directions were $\gamma_T = \gamma_R = 0°$, the antenna orientations were $\theta_T = \theta_R = 90°$, $\psi_T = \psi_R = 0°$, $\Delta_H = 0$. The same parameters are used for all analytical results in Fig. 7. The rest of the parameters in the reference model, i.e, $K = 1.5$, $\mu_T = 0°$, $k_T = 4$, $\beta_{T_m} = 15°$, $R_{t1} = R_{r1} = 9.6$ m, $R_{t2} = R_{r2} = 96$ m, $\mu_R = 180°$, $k_R = 4$, $\beta_{R_m} = 15°$, $\eta_T = \eta_R = 0.3$, and $\eta_{TR} = 0.4$, are manually estimated to match the SISO sD-psd in Fig. 4(d) of [7], and are summarized in Column VII of Table II. Fig. 7 shows the close agreement between the theoretical and empirical SISO sD-psds. Furthermore, we can observe that this spectrum is similar to the U-shaped spectrum of cellular channels. This is not surprising result because the SBT and SBR rays are prevalent (i.e., $\eta_T = \eta_R = 0.3$, and $\eta_{TR} = 0.4$) when the vehicles are driven very close to the sound blockers on the edge of the highway. To illustrate the importance of combining the DB, SBT, and SBR rays, Fig. 7 also plots the SISO sD-psd with only DB and LoS rays. The results show that the model with only DB and LoS rays has a sD-psd with a significantly different shape as compared to the model with SBT, SBR, DB, and LoS rays. Furthermore, Fig. 7 shows that the 2-D model (i.e, $\beta_{T_m} = \beta_{R_m} = 0°$) underestimates the sD-psd. Finally, Fig. 7 plots the MIMO sD-psd, $S_{11,22}(\nu)$, for the antenna elements separation of $d_T = d = R = 1\lambda$ and again shows that the sD-psd decreases with increased antenna element separation. Recently, we conducted the MIMO M-to-M channel-sounding experimental campaign along surface streets and on the Interstate highways in the Midtown Atlanta metropolitan area. The experimental campaign and the detailed verification of the reference model in terms of the CDF, STF-CFs, sD-psds, psds, and LCR are presented in [15]. The results in [15] along with those in Figs. 6 and 7 validate the utility of our 3-D parametric reference model.

C. psds

The psds of the time-variant transfer function is the inverse Fourier transform of the space-frequency correlation function $R_{pq,\tilde{p}\tilde{q}}(\Delta t = 0, \Delta f)$. From (25), it follows that the psds is a summation of the psds functions of the SBT, SBR, DB, and LoS components. Appendix E shows that the psds of the LoS, SBT, SBR and DB components are, respectively,

$$P^{LoS}_{pq,\tilde{p}\tilde{q}}(\tau_{\mathrm{rel}}) = \mathcal{F}^{-1}_{\Delta f}\{R^{LoS}_{pq,\tilde{p}\tilde{q}}(\Delta t = 0, \Delta f)\}$$
$$= K e^{j\frac{2\pi}{\lambda}[(p-\tilde{p})d_{Tx} - (q-\tilde{q})d_{Rx}]}\delta(\tau - \sqrt{(D^2 + \Delta_H^2)/c_0^2}), \quad (51)$$

$$P^{SBT}_{pq,\tilde{p}\tilde{q}}(\tau_{\mathrm{rel}}) = \mathcal{F}^{-1}_{\Delta f}\{R^{SBT}_{pq,\tilde{p}\tilde{q}}(\Delta t = 0, \Delta f)\} = \frac{\eta_T}{I_0(k_T)}$$
$$\times \frac{\cos\left(\frac{2\pi}{\lambda}\beta_{T_m}(p-\tilde{p})d_{Tz}\right)}{1 - \left(\frac{4\beta_{T_m}(p-\tilde{p})d_{Tz}}{\lambda}\right)^2} e^{-j\frac{2\pi}{\lambda}(q-\tilde{q})d_{Rx}} \frac{2}{R_{t2}^2 - R_{t1}^2}$$
$$\times \int_{R_{ta}}^{R_{tb}} \left(1 - \gamma\frac{R_t}{D}\right) R_t e^{j\frac{2\pi}{c_0}R_t B_{SBT}(c_0\tau_{\mathrm{rel}}/R_t - 1)}$$
$$\times \frac{\cosh\left(2jC_{SBT}\sqrt{\frac{c_0\tau_{\mathrm{rel}}}{2R_t}\left(1 - \frac{c_0\tau_{\mathrm{rel}}}{2R_t}\right)}\right)}{\frac{2\pi}{c_0}R_t\sqrt{\frac{c_0\tau_{\mathrm{rel}}}{2R_t}\left(1 - \frac{c_0\tau_{\mathrm{rel}}}{2R_t}\right)}} dR_t, \quad (52)$$

$$P^{SBR}_{pq,\tilde{p}\tilde{q}}(\tau_{\mathrm{rel}}) = \mathcal{F}^{-1}_{\Delta f}\{R^{SBR}_{pq,\tilde{p}\tilde{q}}(\Delta t = 0, \Delta f)\} = \frac{\eta_R}{I_0(k_R)}$$
$$\times \frac{\cos\left(\frac{2\pi}{\lambda}\beta_{R_m}(q-\tilde{q})d_{Rz}\right)}{1 - \left(\frac{4\beta_{R_m}(q-\tilde{q})d_{Rz}}{\lambda}\right)^2} e^{j\frac{2\pi}{\lambda}(p-\tilde{p})d_{Tx}} \frac{2}{R_{r2}^2 - R_{r1}^2}$$

$$\times \int_{R_{ra}}^{R_{rb}} \left(1-\gamma\frac{R_r}{D}\right) R_r e^{j\frac{2\pi}{c_0}R_r B_{SBR}(c_0\tau_{\mathrm{rel}}/R_r-1)} \times \frac{\cosh\left(2jC_{SBR}\sqrt{\frac{c_0\tau_{\mathrm{rel}}}{2R_r}\left(1-\frac{c_0\tau_{\mathrm{rel}}}{2R_r}\right)}\right)}{\frac{2\pi}{c_0}R_r\sqrt{\frac{c_0\tau_{\mathrm{rel}}}{2R_r}\left(1-\frac{c_0\tau_{\mathrm{rel}}}{2R_r}\right)}} dR_r, \quad (53)$$

$$P^{DB}_{pq,\tilde{p}\tilde{q}}(\tau_{\mathrm{rel}}) = \mathcal{F}^{-1}_{\Delta f}\{R^{DB}_{pq,\tilde{p}\tilde{q}}(\Delta t=0,\Delta f)\} = \frac{\eta_{TR}}{I_0(k_T)I_0(k_R)} \times \frac{\cos\left(\frac{2\pi}{\lambda}\beta_{T_m}(p-\tilde{p})d_{Tz}\right)}{1-\left(\frac{4\beta_{T_m}(p-\tilde{p})d_{Tz}}{\lambda}\right)^2} \frac{\cos\left(\frac{2\pi}{\lambda}\beta_{R_m}(q-\tilde{q})d_{Rz}\right)}{1-\left(\frac{4\beta_{R_m}(q-\tilde{q})d_{Rz}}{\lambda}\right)^2} \times \frac{2}{(R^2_{t2}-R^2_{t1})(R^2_{r2}-R^2_{r1})}\Bigg[\int_{R_{ta}}^{R_{tb}} R_t e^{j\frac{2\pi}{c_0}R_t B_{DB}(\frac{c_0\tau_{\mathrm{rel}}}{R_t}-1)} \times \frac{\cosh\left(2jC_{DB}\sqrt{\frac{c_0\tau_{\mathrm{rel}}}{2R_t}\left(1-\frac{c_0\tau_{\mathrm{rel}}}{2R_t}\right)}\right)}{\frac{2\pi}{c_0}R_t\sqrt{\frac{c_0\tau_{\mathrm{rel}}}{2R_t}\left(1-\frac{c_0\tau_{\mathrm{rel}}}{2R_t}\right)}} dR_t \odot \int_{R_{ra}}^{R_{rb}}\left(1-\gamma\frac{R_r}{D}\right)R_r \times \frac{e^{j\frac{2\pi}{c_0}R_r D_{DB}(\frac{c_0\tau_{\mathrm{rel}}}{R_r}-1)}\cosh\left(2jE_{DB}\sqrt{\frac{c_0\tau_{\mathrm{rel}}}{2R_r}\left(1-\frac{c_0\tau_{\mathrm{rel}}}{2R_r}\right)}\right)}{\frac{2\pi}{c_0}R_r\sqrt{\frac{c_0\tau_{\mathrm{rel}}}{2R_r}\left(1-\frac{c_0\tau_{\mathrm{rel}}}{2R_r}\right)}} dR_r + \int_{R_{ta}}^{R_{tb}}\left(1-\gamma\frac{R_t}{D}\right)R_t \frac{\cosh\left(2jC_{DB}\sqrt{\frac{c_0\tau_{\mathrm{rel}}}{2R_t}\left(1-\frac{c_0\tau_{\mathrm{rel}}}{2R_t}\right)}\right)}{\frac{2\pi}{c_0}R_t\sqrt{\frac{c_0\tau_{\mathrm{rel}}}{2R_t}\left(1-\frac{c_0\tau_{\mathrm{rel}}}{2R_t}\right)}} \times e^{j\frac{2\pi}{c_0}R_t B_{DB}(\frac{c_0\tau_{\mathrm{rel}}}{R_t}-1)} dR_t \odot \int_{R_{ra}}^{R_{rb}} R_r e^{j\frac{2\pi}{c_0}R_r D_{DB}(\frac{c_0\tau_{\mathrm{rel}}}{R_r}-1)} \times \frac{\cosh\left(2jE_{DB}\sqrt{\frac{c_0\tau_{\mathrm{rel}}}{2R_r}\left(1-\frac{c_0\tau_{\mathrm{rel}}}{2R_r}\right)}\right)}{\frac{2\pi}{c_0}R_r\sqrt{\frac{c_0\tau_{\mathrm{rel}}}{2R_r}\left(1-\frac{c_0\tau_{\mathrm{rel}}}{2R_r}\right)}} dR_r\Bigg], \quad (54)$$

where $\cosh(\cdot)$ is the hyperbolic cosine, $\odot$ denotes convolution, $\delta(\cdot)$ denotes the Dirac delta function, and $\tau_{\mathrm{rel}} = \tau - D/c_0$. The integrals in (52)–(54) need to be numerically evaluated over the range of possible radii R_t and R_r. For the range $0 \le \tau_{\mathrm{rel}} \le 2R_{t1}/c_0$, the integration limits are $R_{ta} = R_{t1}$, $R_{tb} = R_{t2}$, $R_{ra} = R_{r1}$, and $R_{rb} = R_{r2}$. On the other hand, when $2R_{t1}/c_0 \le \tau_{\mathrm{rel}} \le 2R_{t2}/c_0$, the integration limits are $R_{ta} = c_0\tau_{\mathrm{rel}}/2$, $R_{tb} = R_{t2}$, $R_{ra} = c_0\tau_{\mathrm{rel}}/2$, and $R_{rb} = R_{r2}$. Finally, the parameters in (52) and (53) are defined in (96), whereas the parameters in (54) are defined in (99). Note that existing power delay spectra derived assuming "one-circular-ring" model [25], are special cases of (53). For example, the 2-D non-isotropic power delay spectrum in [25] is obtained for $\beta_{R_m} = 0$, $\psi_R = 0$, and $d_T = d_R = 0$.

Figs. 8 and 9 show several SISO and MIMO psds that can be found in highway environments and compares them with the measured SISO psds in [8]. The measurements in [8] were performed on the highway, at 2.4 GHz, and the maximum Doppler frequencies were $f_{T\max} = f_{R\max} = 200$ Hz. The vehicles were driven in the rightmost lane of the highway and the sound blockers on the edge of the highway were periodically present. Both, the $\mathrm{T_x}$ and $\mathrm{R_x}$ were equipped with one omnidirectional antenna. The distance between the

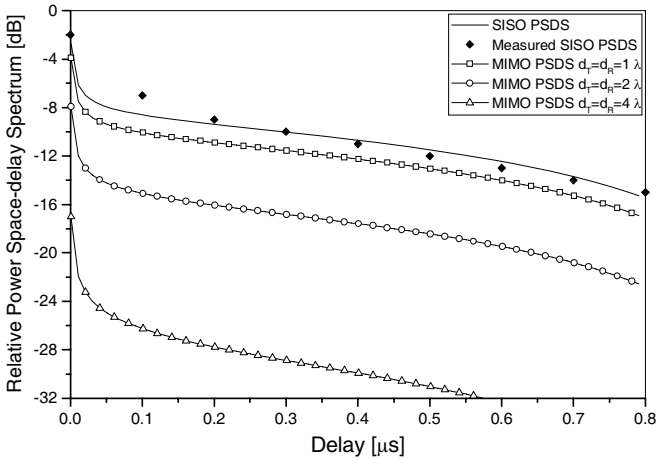

Fig. 8. The theoretical and measured psds in the rightmost lane of an Interstate highway *without* sound blockers.

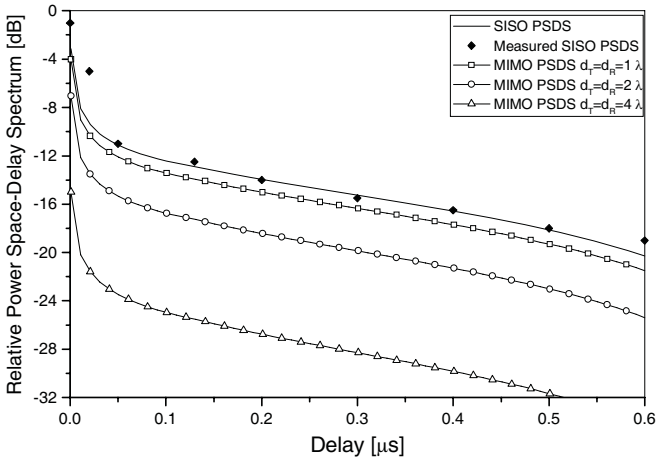

Fig. 9. The theoretical and measured psds in the rightmost lane of an Interstate highway *with* sound blockers.

$\mathrm{T_x}$ and $\mathrm{R_x}$ was approximately $D = 300$ m. The moving directions were $\gamma_T = \gamma_R = 90°$, the antenna orientations were $\theta_T = \theta_R = \psi_T = \psi_R = 0°$, and the antenna elevations were $\Delta_H = 0$. The same parameters are used to obtain all analytical results in Figs. 8 and 9. The measured SISO psds in Fig. 8 is obtained on the part of the highway without sound blockers. The estimated parameters in Fig. 8 summarized in Column VIII of Table II. Fig. 8 shows the close agreement between the theoretical and empirical SISO psds. The results show that DB rays are prevalent on the part of the highway without sound blockers (i.e., $\eta_T = \eta_R = 0.2$, and $\eta_{TR} = 0.6$). In this case, the psds closely follows the one-sided exponential function dies out after 0.8 μs.

The measured SISO psds in Fig. 9 is obtained on the part of the highway with sound blockers. The estimated parameters in Fig. 9 are summarized in Column IX of Table II. Fig. 9 shows the close agreement between the theoretical and empirical SISO psds. The results show that SBT and SBR rays are prevalent on the part of the highway with sound blockers (i.e., $\eta_T = \eta_R = 0.45$, and $\eta_{TR} = 0.1$). We can observe that this psds does not follow the one-sided exponential function, which is characteristic for F-to-M cellular channels. The M-

to-M psds has two distinct slopes and dies out after 0.6 μs. Figs. 8 and 9 also show several MIMO psds, $P_{11,22}(\tau_{\rm rel})$, with $d_T = d_R = \{1\lambda, 2\lambda, 4\lambda\}$. The results show that the psds decreases with increased antenna element separation. Again, the results in [15] and Figs. 8 and 9 confirm the utility of the proposed wideband model.

IV. Wideband MIMO Mobile-to-Mobile Simulation Model

The reference model for wideband MIMO M-to-M channel described in Section II assumes an infinite number of scatterers, which prevents practical implementation. It is desirable to design simulation model with a finite (preferably small) number of scatterers, while still matching the statistical properties of the reference model.

Assuming 3-D non-isotropic scattering and using the reference model described in Section II, and using the results in [14], we propose the following function as a time-variant transfer function: $T_{pq}(t,f) = T_{pq}^{(I)}(t,f) + jT_{pq}^{(Q)}(t,f)$ where

$$
\begin{aligned}
T_{pq}^{(I)}(t,f) &= \frac{\rho_{SBT}}{\sqrt{M}} \sum_{l,m,i=1}^{L,M_A^{(l)},M_E^{(l)}} \left(1 - \frac{\gamma}{2}\frac{R_t^{(l)}}{D}\right) \cos\Big[K_p D_T^{SBT} \\
&+ K_q D_R^{SBT} + 2\pi t f_{T\max} \cos\left(\alpha_T^{(m,l)} - \gamma_T\right) \cos\beta_T^{(i,l)} + \phi_{m,i,l} \\
&+ 2\pi t f_{R\max}\Big(\cos\gamma_R - \Delta_T^{(l)} \sin\gamma_R \sin\alpha_T^{(m,l)}\Big) \cos\left(\Delta_T^{(l)}\beta_T^{(i,l)}\right) \\
&- \frac{2\pi}{c_0} f\Big(D + R_t^{(l)}\Big(1 - \cos\alpha_T^{(m,l)}\Big)\Big)\Big] + \frac{\rho_{SBR}}{\sqrt{N}} \sum_{k,n,g=1}^{F,N_A^{(k)},N_E^{(k)}} \left(1 - \frac{\gamma}{2}\frac{R_r^{(k)}}{D}\right) \\
&\times \cos\Big[K_p D_T^{SBR} + K_q D_R^{SBR} + 2\pi t f_{R\max}\cos\Big(\alpha_R^{(n,k)} - \gamma_R\Big) \\
&\times \cos\beta_R^{(g,k)} + \phi_{n,g,k} + 2\pi t f_{T\max}\Big(\Delta_R^{(k)}\sin\gamma_T \sin\alpha_R^{(n,k)} + \cos\gamma_T\Big) \\
&\times \cos\left(\Delta_R^{(k)}\beta_R^{(g,k)}\right) - \frac{2\pi}{c_0} f\Big(D + R_r^{(k)}\Big(1 + \cos\alpha_R^{(n,k)}\Big)\Big)\Big] \\
&+ \frac{\rho_{DB}}{\sqrt{MN}} \sum_{l,m,i=1}^{L,M_A^{(l)},M_E^{(l)}F,N_A^{(k)},N_E^{(k)}} \sum_{k,n,g=1} \left(1 - \frac{\gamma}{2}\frac{R_t^{(l)} + R_r^{(k)}}{2D}\right) \cos\Big[K_p D_T^{DB} \\
&+ K_q D_R^{DB} + 2\pi t f_{T\max}\cos\Big(\alpha_T^{(m,l)} - \gamma_T\Big) \cos\beta_T^{(i,l)} + 2\pi t f_{R\max} \\
&\times \cos\left(\alpha_R^{(n,k)} - \gamma_R\right) \cos\beta_R^{(g,k)} - \frac{2\pi}{c_0} f\Big(D + R_t^{(l)}\Big(1 - \cos\alpha_T^{(m,l)}\Big) \\
&+ R_r^{(k)}\Big(1 + \cos\alpha_R^{(n,k)}\Big)\Big) + \phi_{m,i,l,n,g,k}\Big] + \rho_{LoS} \\
&\times \cos\left[2\pi t\left(f_T^{LoS} + f_R^{LoS}\right) - \frac{2\pi}{c_0} f\sqrt{D^2 + {\Delta_H}^2}\right. \\
&\left. + K_p d_{Tx} + K_q d_R \cos\psi_R \cos(\alpha_{Rq}^{LoS} - \theta_R)\right], \qquad (55)
\end{aligned}
$$

$$
\begin{aligned}
T_{pq}^{(Q)}(t,f) &= \frac{\rho_{SBT}}{\sqrt{M}} \sum_{l,m,i=1}^{L,M_A^{(l)},M_E^{(l)}} \left(1 - \frac{\gamma}{2}\frac{R_t^{(l)}}{D}\right) \sin\Big[K_p D_T^{SBT} \\
&+ K_q D_R^{SBT} + 2\pi t f_{T\max} \cos\left(\alpha_T^{(m,l)} - \gamma_T\right) \cos\beta_T^{(i,l)} + \phi_{m,i,l} \\
&+ 2\pi t f_{R\max}\Big(\cos\gamma_R - \Delta_T^{(l)} \sin\gamma_R \sin\alpha_T^{(m,l)}\Big) \cos\left(\Delta_T^{(l)}\beta_T^{(i,l)}\right) \\
&- \frac{2\pi}{c_0} f\Big(D + R_t^{(l)}\Big(1 - \cos\alpha_T^{(m,l)}\Big)\Big)\Big] + \frac{\rho_{SBR}}{\sqrt{N}} \sum_{k,n,g=1}^{F,N_A^{(k)},N_E^{(k)}} \left(1 - \frac{\gamma}{2}\frac{R_r^{(k)}}{D}\right) \\
&\times \sin\Big[K_p D_T^{SBR} + K_q D_R^{SBR} + 2\pi t f_{R\max}\cos\Big(\alpha_R^{(n,k)} - \gamma_R\Big) \\
&\times \cos\beta_R^{(g,k)} + \phi_{n,g,k} + 2\pi t f_{T\max}\Big(\Delta_R^{(k)}\sin\gamma_T \sin\alpha_R^{(n,k)} + \cos\gamma_T\Big) \\
&\times \cos\left(\Delta_R^{(k)}\beta_R^{(g,k)}\right) - \frac{2\pi}{c_0} f\Big(D + R_r^{(k)}\Big(1 + \cos\alpha_R^{(n,k)}\Big)\Big)\Big] \\
&+ \frac{\rho_{DB}}{\sqrt{MN}} \sum_{l,m,i=1}^{L,M_A^{(l)},M_E^{(l)}F,N_A^{(k)},N_E^{(k)}} \sum_{k,n,g=1} \left(1 - \frac{\gamma}{2}\frac{R_t^{(l)} + R_r^{(k)}}{2D}\right) \sin\Big[K_p D_T^{DB} \\
&+ K_q D_R^{DB} + 2\pi t f_{T\max}\cos\Big(\alpha_T^{(m,l)} - \gamma_T\Big) \cos\beta_T^{(i,l)} + 2\pi t f_{R\max} \\
&\times \cos\Big(\alpha_R^{(n,k)} - \gamma_R\Big) \cos\beta_R^{(g,k)} - \frac{2\pi}{c_0} f\Big(D + R_t^{(l)}\Big(1 - \cos\alpha_T^{(m,l)}\Big) \\
&+ R_r^{(k)}\Big(1 + \cos\alpha_R^{(n,k)}\Big)\Big) + \phi_{m,i,l,n,g,k}\Big] + \rho_{LoS} \\
&\times \sin\left[2\pi t\left(f_T^{LoS} + f_R^{LoS}\right) - \frac{2\pi}{c_0} f\sqrt{D^2 + {\Delta_H}^2} + K_p d_{Tx}\right. \\
&\left. + K_q d_R \cos\psi_R \cos(\alpha_{Rq}^{LoS} - \theta_R)\right], \qquad (56)
\end{aligned}
$$

are the in-phase (I) and quadrature (Q) components of the time-variant transfer function, $M = \sum_{l=1}^{L} M^{(l)} = \sum_{l=1}^{L} M_A^{(l)} M_E^{(l)}$, $N = \sum_{k=1}^{F} N^{(k)} = \sum_{k=1}^{F} N_A^{(k)} N_E^{(k)}$, $\rho_{SBT} = \sqrt{\eta_T/(K+1)}$, $\rho_{SBR} = \sqrt{\eta_R/(K+1)}$, $\rho_{DB} = \sqrt{\eta_{TR}/(K+1)}$, $\rho_{LoS} = \sqrt{K/(1+K)}$, $K_p = \pi(L_t + 1 - 2p)/\lambda$, $K_q = \pi(L_r + 1 - 2q)/\lambda$, $D_T^{SBT} = d_{Tx}\cos\alpha_T^{(m,l)} + d_{Ty}\sin\alpha_T^{(m,l)} + d_{Tz}\sin\beta_T^{(i,l)}$, $D_R^{SBT} = d_{Ry}\Delta_T^{(l)}\sin\alpha_T^{(m,l)} - d_{Rx}$, $D_R^{SBR} = d_{Rx}\cos\alpha_R^{(n,k)} + d_{Ry}\sin\alpha_R^{(n,k)} + d_{Rz}\sin\beta_R^{(g,k)}$, $D_T^{SBR} = d_{Ty}\Delta_R^{(k)}\sin\alpha_R^{(n,k)} + d_{Tx}$, $D_T^{DB} = d_{Tx}\cos\alpha_T^{(m,l)} + d_{Ty}\sin\alpha_T^{(m,l)} + d_{Tz}\sin\beta_T^{(i,l)}$, $D_R^{DB} = d_{Rx}\cos\alpha_R^{(n,k)} + d_{Ry}\sin\alpha_R^{(n,k)} + d_{Rz}\sin\beta_R^{(g,k)}$, $f_T^{LoS} = f_{T\max}\cos(\pi - \alpha_{Rq}^{LoS} - \gamma_T)$, and $f_R^{LoS} = f_{R\max}\cos(\alpha_{Rq}^{LoS} - \gamma_R)$. Note that the input delay-spread function can be obtained as the inverse Fourier transform of the time-variant transfer function, i.e., $h_{pq}(t,\tau) = \mathcal{F}_f^{-1}\{T_{pq}(t,f)\}$.

The AAoDs, $\alpha_T^{(m,l)}$, and the AAoAs, $\alpha_R^{(n,k)}$, are modelled using the von Mises pdf in (22) and are generated as follows:

$$\alpha_T^{(m,l)} = F^{-1}\left(\frac{m - 0.5}{M_A^{(l)}}\right), \qquad (57)$$

$$\alpha_R^{(n,k)} = F^{-1}\left(\frac{n - 0.5}{N_A^{(k)}}\right), \qquad (58)$$

for $m = 1, \ldots, M_A^{(l)}$, $n = 1, \ldots, N_A^{(k)}$, where $F(\cdot)^{-1}$ denotes the inverse cumulative von Mises distribution function and is evaluated using method in [**?**]. The EAoDs, $\beta_T^{(i,l)}$, and the EAoAs, $\beta_R^{(g,k)}$, are modelled using the pdf in (23) and are generated as follows:

$$\beta_T^{(i,l)} = \frac{2\beta_{T_m}}{\pi}\arcsin\left(\frac{2i - 1}{M_E^{(l)}} - 1\right), \qquad (59)$$

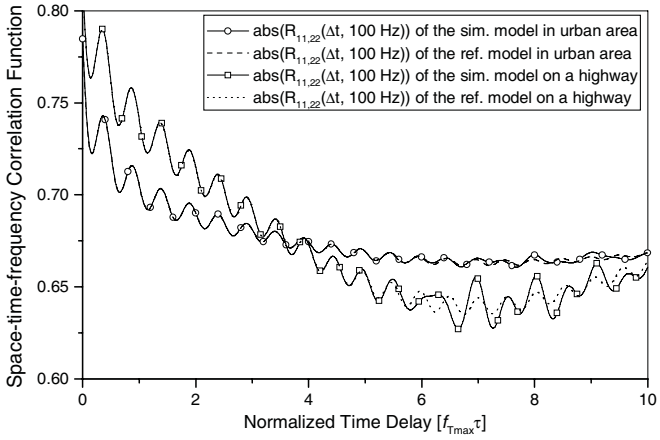

Fig. 10. The simulated and theoretical STF-CFs in the USS and IH environments.

$$\beta_R^{(g,k)} = \frac{2\beta_{R_m}}{\pi}\arcsin\left(\frac{2g-1}{N_E^{(k)}}-1\right), \quad (60)$$

for $i = 1, \ldots, M_E^{(l)}$, $g = 1, \ldots, N_E^{(k)}$. The radii $R_t^{(l)}$ and $R_r^{(k)}$ are modelled using the pdfs $f(R_t) = 2R_t/(R_{t2}^2 - R_{t1}^2)$ and $f(R_r) = 2R_r/(R_{r2}^2 - R_{r1}^2)$, respectively, and are generated as follows:

$$R_t^{(l)} = \sqrt{\frac{(l-0.5)(R_{t2}^2 - R_{t1}^2)}{L} + R_{t1}^2}, \quad (61)$$

$$R_r^{(k)} = \sqrt{\frac{(k-0.5)(R_{r2}^2 - R_{r1}^2)}{F} + R_{r1}^2}, \quad (62)$$

for $l = 1, \ldots, L$, $k = 1, \ldots, F$. The phases $\phi_{m,i,l}$, $\phi_{n,g,k}$, and $\phi_{m,i,l,n,g,k}$ are generated as independent uniform random variables on the interval $[-\pi, \pi)$.

For $M, N \to \infty$, our simulation model has the same STF-CF as that of the reference model in (25). The derivations are omitted for brevity. Fig. 10 compares the simulated STF-CF obtained using (55) and (56) and the STF-CF of the reference model in (25), assuming the 3-D non-isotropic radio propagation ($k_T = k_R = 2$, $\beta_{T_m} = \beta_{R_m} = 15°$) in the urban and highway environments. In the urban environment, the double-bounced rays bear more energy than the single-bounced rays ($\eta_T = \eta_R = 0.1$, $\eta_{TR} = 0.8$), whereas, on the highways, the single-bounced rays are prevalent ($\eta_T = \eta_R = 0.45$, $\eta_{TR} = 0.1$). In all simulations, we use a normalized sampling period $f_T T_s = 0.01$ ($f_{Tmax} = f_{Rmax}$), assume $L_t = L_r = 2$ antennas, use $M_A^{(l)} = 44$, $M_E^{(l)} = 9$, $N_A^{(k)} = 44$, and $N_E^{(k)} = 9$ scatterers and six tap-delays ($L = 3$ and $K = 3$). All parameters used to obtain the curves in Fig. 10 are summarized in the last column of Table II. Results show that the STF-CF of the simulation model closely matches that of the reference model in the range of normalized time delays, $0 \le f_{T\max} T_s \le 6$.

V. Conclusions

This paper proposed a three-dimensional geometrical propagation model for wideband MIMO M-to-M multipath fading channels. Based on the geometrical model, a parametric reference model was proposed for MIMO M-to-M Ricean fading channels. From the reference model, the STF-CF was derived for a 3-D non-isotropic scattering environment. It was shown that the time and frequency dispersion of the WSSUS channel cannot be treated independently. Furthermore, the sD-psd and the psds were derived and compared with measured data. The close agreement between the theoretical and empirical curves confirms the utility of the proposed wideband model. Finally, a new SoS based simulation model for wideband MIMO M-to-M Ricean fading channels was proposed. The statistics of the simulation models have been verified by simulation. The results show that the simulation model closely approximates the reference model.

Acknowledgment

The authors would like to thank the anonymous reviewers whose feedback helped improve the quality of this paper.

Appendix A
Angles of Arrival and Angles of Departure for Single-bounced Rays

Applying the sine law to the triangles $\triangle O_T S_T^{(m)'} O_R$ and $\triangle O_T S_R^{(n)'} O_R$, respectively, we obtain following identities

$$\frac{D}{\sin\left(\pi - \alpha_T^{(m,l)} - \left(\pi - \alpha_R^{(m,l)}\right)\right)} = \frac{R_t^{(l)}}{\sin\left(\pi - \alpha_R^{(m,l)}\right)}, \quad (63)$$

$$\frac{D}{\sin\left(\pi - \alpha_T^{(n,k)} - \left(\pi - \alpha_R^{(n,k)}\right)\right)} = \frac{R_r^{(k)}}{\sin\alpha_T^{(n,k)}}. \quad (64)$$

From Fig. 2, we observe that $\pi - \alpha_R^{(m,l)} \le \arcsin(R_t^{(l)}/D)$ and $\alpha_T^{(n,k)} \le \arcsin(R_r^{(k)}/D)$. Based on the assumption $\min\{R_{t2}, R_{r2}\} \ll D$, we conclude that $\arcsin(R_t^{(l)}/D) \approx R_t^{(l)}/D = \Delta_T^{(l)}$ and $\arcsin(R_r^{(k)}/D) \approx R_r^{(k)}/D = \Delta_R^{(k)}$, and consequently $\pi - \alpha_R^{(m,l)}$ and $\alpha_T^{(n,k)}$ are small angles. Using (63) and (64), and the approximations $\sin x \approx x$ and $\cos x \approx 1$ for small x, we derive the following approximations for the azimuth angles of arrival and departure, respectively,

$$\alpha_R^{(m,l)} \approx \pi - \Delta_T^{(l)}\sin\alpha_T^{(m,l)}, \quad (65)$$

$$\alpha_T^{(n,k)} \approx \Delta_R^{(k)}\sin\alpha_R^{(n,k)}. \quad (66)$$

Furthermore, using (65) and (66), we obtain the following approximations

$$\cos\left(\alpha_R^{(m,l)} - \gamma_R\right) \approx -\cos\gamma_R + \Delta_T^{(l)}\sin\gamma_R\sin\alpha_T^{(m,l)}, \quad (67)$$

$$\cos\left(\alpha_T^{(n,k)} - \gamma_T\right) \approx \cos\gamma_T + \Delta_R^{(k)}\sin\gamma_T\sin\alpha_R^{(n,k)}. \quad (68)$$

Finally, observing Fig. 2, we obtain the following identities

$$R_r^{(k)}\tan\beta_R^{(n,k)} - \Delta_H = \left(D + R_r^{(k)}\right)\tan\beta_T^{(n,k)}, \quad (69)$$

$$R_t^{(l)}\tan\beta_T^{(m,l)} + \Delta_H = \left(D - R_t^{(l)}\right)\tan\left(\pi - \beta_R^{(m,l)}\right), \quad (70)$$

where $\Delta_H = h_T - h_R$. Using (69) and (70), the assumption $\min\{R_{t2}, R_{r2}\} \ll D$, and approximations $\sin x \approx x$ and $\cos x \approx 1$ for small x, we derive the following approximations for the elevation angles of arrival and departure, respectively,

$$\beta_R^{(m,l)} \approx \pi - \left(\Delta_T^{(l)}\beta_T^{(m,l)} + \Delta_H/D\right), \quad (71)$$

$$\beta_T^{(n,k)} \approx \Delta_R^{(k)}\beta_R^{(n,k)} - \Delta_H/D. \quad (72)$$

APPENDIX B
THE SBT, SBR, DB, AND LOS COMPONENTS OF THE TIME-VARIANT TRANSFER FUNCTION

Using (1) - (20), the SBT, SBR, DB, and LoS components of the time-variant transfer function in (21) can be written as

$$T_{pq}^{SBT}(t,f)=\mathcal{F}_\tau\left\{h_{pq}^{SBT}(t,\tau)\right\}=\Omega_{pq}\sqrt{\frac{\eta_T}{K+1}}\lim_{M\to\infty}\sum_{l=1}^{L}$$
$$\sum_{m=1}^{M^{(l)}}\frac{\left(1-\frac{\gamma}{2}\Delta_T^{(l)}\right)}{\sqrt{M}}a_{p,m,l}^{SBT}b_{q,m,l}^{SBT}e^{j2\pi tf_{T\max}\cos(\alpha_T^{(m,l)}-\gamma_T)\cos\beta_T^{(m,l)}}$$
$$e^{j2\pi tf_{R\max}(\cos\gamma_R-\Delta_T^{(l)}\sin\gamma_R\sin\alpha_T^{(m,l)})\cos(\Delta_T^{(l)}\beta_T^{(m,l)}+\frac{\Delta_H}{D})}$$
$$e^{-j\frac{2\pi}{c_0\cos\beta_T^{(m,l)}}f\left[D+R_t^{(l)}(1-\cos\alpha_T^{(m,l)})\right]+j\phi_{m,l}}, \quad (73)$$

$$T_{pq}^{SBR}(t,f)=\mathcal{F}_\tau\left\{h_{pq}^{SBR}(t,\tau)\right\}=\Omega_{pq}\sqrt{\frac{\eta_R}{K+1}}\lim_{N\to\infty}\sum_{k=1}^{F}$$
$$\sum_{n=1}^{N^{(k)}}\frac{\left(1-\frac{\gamma}{2}\Delta_R^{(k)}\right)}{\sqrt{N}}a_{p,n,k}^{SBR}b_{q,n,k}^{SBR}e^{j2\pi tf_{R\max}\cos(\alpha_R^{(n,k)}-\gamma_R)\cos\beta_R^{(n,k)}}$$
$$e^{j2\pi tf_{T\max}(\Delta_R^{(k)}\sin\gamma_T\sin\alpha_R^{(n,k)}+\cos\gamma_T)\cos(\Delta_R^{(k)}\beta_R^{(n,k)}-\frac{\Delta_H}{D})}$$
$$e^{-j\frac{2\pi}{c_0\cos\beta_R^{(n,k)}}f\left[D+R_r^{(k)}\left(1+\cos\alpha_R^{(n,k)}\right)\right]+j\phi_{n,k}}, \quad (74)$$

$$T_{pq}^{DB}(t,f)=\mathcal{F}_\tau\left\{h_{pq}^{DB}(t,\tau)\right\}=\Omega_{pq}\sqrt{\frac{\eta_{TR}}{K+1}}$$
$$\lim_{M,N\to\infty}\sum_{l,m=1}^{L,M^{(l)}}\sum_{k,n=1}^{F,N^{(k)}}\frac{\left(1-\frac{\gamma}{4}\Delta_T^{(l)}-\frac{\gamma}{4}\Delta_R^{(k)}\right)}{\sqrt{MN}}a_{p,m,l}^{DB}b_{q,n,k}^{DB}$$
$$e^{j2\pi t\left[f_{T\max}\cos(\alpha_T^{(m,l)}-\gamma_T)\cos\beta_T^{(m,l)}+f_{R\max}\cos(\alpha_R^{(n,k)}-\gamma_R)\cos\beta_R^{(n,k)}\right]}$$
$$e^{-j\frac{2\pi}{c_0}f\left[D+\frac{R_t^{(l)}(1-\cos\alpha_T^{(m,l)})}{\cos\beta_T^{(m,l)}}+\frac{R_r^{(k)}(1+\cos\alpha_R^{(n,k)})}{\cos\beta_R^{(n,k)}}\right]+j\phi_{m,l,n,k}}, \quad (75)$$

$$T_{pq}^{LoS}(t,f)=\mathcal{F}_\tau\left\{h_{pq}^{LoS}(t,\tau)\right\}=\Omega_{pq}\sqrt{\frac{K}{1+K}}$$
$$e^{j2\pi t\left[f_{T\max}\cos\left(\pi-\alpha_{Rq}^{LoS}-\gamma_T\right)+f_{R\max}\cos\left(\alpha_{Rq}^{LoS}-\gamma_R\right)\right]-j\frac{2\pi}{\lambda}D}$$
$$e^{j\frac{\pi}{\lambda}\left[(L_t+1-2p)d_T\cos\theta_T\cos\psi_T+(L_r+1-2q)d_R\cos\psi_R\cos(\alpha_{Rq}^{LoS}-\theta_R)\right]}$$
$$e^{-j\frac{2\pi}{c_0}f\sqrt{D^2+\Delta_H{}^2}}, \quad (76)$$

where the parameters $a_{p,m,l}^{SBT}$, $b_{q,m,l}^{SBT}$, $a_{p,n,k}^{SBR}$, $b_{q,n,k}^{SBR}$, $a_{p,m,l}^{DB}$, and $b_{q,n,k}^{DB}$ are, respectively,

$$a_{p,m,l}^{SBT}\approx e^{j\frac{2\pi}{\lambda}(0.5L_t+0.5-p)d_{Tx}\cos\alpha_T^{(m,l)}\cos\beta_T^{(m,l)}}$$
$$\times\ e^{j\frac{2\pi}{\lambda}(0.5L_t+0.5-p)\left[d_{Ty}\sin\alpha_T^{(m,l)}\cos\beta_T^{(m,l)}+d_{Tz}\sin\beta_T^{(m,l)}\right]}, \quad (77)$$
$$b_{q,m,l}^{SBT}\approx e^{j\frac{2\pi}{\lambda}(0.5L_r+0.5-q)d_R\cos\psi_R\left[\Delta_T^{(l)}\sin\theta_R\sin\alpha_T^{(m,l)}-\cos\theta_R\right]}$$
$$\times\ e^{-j\frac{2\pi}{\lambda}\left(D+R_t^{(l)}\right)}, \quad (78)$$
$$a_{p,n,k}^{SBR}\approx e^{j\frac{2\pi}{\lambda}(0.5L_t+0.5-p)d_T\cos\psi_T\left[\Delta_R^{(k)}\sin\theta_T\sin\alpha_R^{(n,k)}+\cos\theta_T\right]}$$
$$\times\ e^{-j\frac{2\pi}{\lambda}\left(D+R_r^{(k)}\right)}, \quad (79)$$
$$b_{q,n,k}^{SBR}\approx e^{j\frac{2\pi}{\lambda}(0.5L_r+0.5-q)d_{Rx}\cos\alpha_R^{(n,k)}\cos\beta_R^{(n,k)}}$$
$$\times\ e^{j\frac{2\pi}{\lambda}(0.5L_r+0.5-q)\left[d_{Ry}\sin\alpha_R^{(n,k)}\cos\beta_R^{(n,k)}+d_{Rz}\sin\beta_R^{(n,k)}\right]}, \quad (80)$$
$$a_{p,m,l}^{DB}\approx e^{j\frac{2\pi}{\lambda}(0.5L_t+0.5-p)d_{Tx}\cos\alpha_T^{(m,l)}\cos\beta_T^{(m,l)}}$$
$$\times\ e^{j\frac{2\pi}{\lambda}(0.5L_t+0.5-p)\left[d_{Ty}\sin\alpha_T^{(m,l)}\cos\beta_T^{(m,l)}+d_{Tz}\sin\beta_T^{(m,l)}\right]}$$
$$\times\ e^{-j\frac{2\pi}{\lambda}\left(D/2+R_t^{(l)}\right)}, \quad (81)$$
$$b_{q,n,k}^{DB}\approx e^{j\frac{2\pi}{\lambda}(0.5L_r+0.5-q)d_{Rx}\cos\alpha_R^{(n,k)}\cos\beta_R^{(n,k)}}$$
$$\times\ e^{j\frac{2\pi}{\lambda}(0.5L_r+0.5-q)\left[d_{Ry}\sin\alpha_R^{(n,k)}\cos\beta_R^{(n,k)}+d_{Rz}\sin\beta_R^{(n,k)}\right]}$$
$$\times\ e^{-j\frac{2\pi}{\lambda}\left(D/2+R_r^{(k)}\right)}. \quad (82)$$

APPENDIX C
THE CLOSED-FORM STF-CFS OF THE SBT, SBR, AND DB COMPONENTS

After replacing (8), (9), and (13) with (43) - (45), respectively, calculating the new SBT, SBR and DB components of the time-variant transfer function, using trigonometric transformations, the equality $\int_{-\pi}^{\pi}\exp\{a\sin(c)+b\cos(c)\}dc=2\pi I_0\left(\sqrt{a^2+b^2}\right)$ [13, eq. 3.338-4], and the results in [14], the closed-form STF-CFs of the SBT, SBR and DB components can be written as

$$R_{pq,\tilde{p}\tilde{q}}^{SBT}(\Delta t)R_{pq,\tilde{p}\tilde{q}}^{SBT}(\Delta f)=\frac{\eta_T}{I_0(k_T)}\frac{\cos\left(\frac{2\pi}{\lambda}\beta_{Tm}(p-\tilde{p})d_{Tz}\right)}{1-\left(\frac{4\beta_{Tm}(p-\tilde{p})d_{Tz}}{\lambda}\right)^2}$$
$$\times\ I_{SBT}e^{-j\frac{2\pi}{\lambda}(q-\tilde{q})d_{Rx}}e^{-j2\pi\Delta tf_{R\max}\cos\gamma_R}\frac{e^{-j\frac{2\pi}{c_0}\Delta fD}}{R_{t2}^2-R_{t1}^2}$$
$$\times\ I_0\left(\sqrt{x_{SBT1}^2+y_{SBT1}^2}\right), \quad (83)$$

$$R_{pq,\tilde{p}\tilde{q}}^{SBR}(\Delta t)R_{pq,\tilde{p}\tilde{q}}^{SBR}(\Delta f)=\frac{\eta_R}{I_0(k_R)}\frac{\cos\left(\frac{2\pi}{\lambda}\beta_{Rm}(q-\tilde{q})d_{Rz}\right)}{1-\left(\frac{4\beta_{Rm}(q-\tilde{q})d_{Rz}}{\lambda}\right)^2}$$
$$\times\ I_{SBR}e^{j\frac{2\pi}{\lambda}(p-\tilde{p})d_{Tx}}e^{j2\pi\Delta tf_{T\max}\cos\gamma_T}\frac{e^{-j\frac{2\pi}{c_0}\Delta fD}}{R_{r2}^2-R_{r1}^2}$$
$$\times\ I_0\left(\sqrt{x_{SBR1}^2+y_{SBR1}^2}\right), \quad (84)$$

$$R_{pq,\tilde{p}\tilde{q}}^{DB}(\Delta t)R_{pq,\tilde{p}\tilde{q}}^{DB}(\Delta f)=\frac{\eta_{TR}\cos\left(\frac{2\pi}{\lambda}\beta_{Tm}(p-\tilde{p})d_{Tz}\right)}{I_0(k_T)I_0(k_R)\left[1-\left(\frac{4\beta_{Tm}(p-\tilde{p})d_{Tz}}{\lambda}\right)^2\right]}$$
$$\times\ \frac{\cos\left(\frac{2\pi}{\lambda}\beta_{Rm}(q-\tilde{q})d_{Rz}\right)}{1-\left(\frac{4\beta_{Rm}(q-\tilde{q})d_{Rz}}{\lambda}\right)^2}\frac{e^{-j2\pi\Delta fD/c_0}}{(R_{t2}^2-R_{t1}^2)(R_{r2}^2-R_{r1}^2)} \quad (85)$$
$$\times\ I_0\left(\sqrt{x_{DB1}^2+y_{DB}^2}\right)I_0\left(\sqrt{z_{DB1}^2+w_{DB}^2}\right)(I_{T1}I_{R2}+I_{T2}I_{R1})$$

where $a=2\pi\Delta f/c_0$, $c=\gamma/D$, and

$$x_{SBT1}=j(2\pi/\lambda)(p-\tilde{p})d_{Tx}+j2\pi\Delta tf_{T\max}\cos\gamma_T$$
$$+\ k_T\cos\mu_T,$$
$$y_{SBT1}=j2\pi(p-\tilde{p})d_{Ty}/\lambda+j2\pi(q-\tilde{q})d_{Ry}$$
$$\times\ (R_{t1}+0.5(R_{t2}-R_{t1}))/(D\lambda)+j2\pi\Delta tf_{T\max}\sin\gamma_T$$
$$+\ j2\pi\Delta tf_{R\max}\sin\gamma_R(R_{t1}+0.5(R_{t2}-R_{t1}))/D+k_T\sin\mu_T,$$
$$x_{SBR1}=j(2\pi/\lambda)(q-\tilde{q})d_{Rx}+j2\pi\Delta tf_{R\max}\cos\gamma_R$$
$$+\ k_R\cos\mu_R,$$

$$
\begin{aligned}
&y_{SBR1} = j2\pi(q-\tilde{q})d_{Ry}/\lambda + j2\pi(p-\tilde{p})d_{Ty} \\
&\times (R_{r1} + 0.5(R_{r2}-R_{r1}))/(D\lambda) + j2\pi\Delta t f_{R\max}\sin\gamma_R \\
&+ j2\pi\Delta t f_{T\max}\sin\gamma_T(R_{r1}+0.5(R_{r2}-R_{r1}))/D + k_R\sin\mu_R, \\
&x_{DB1} = j(2\pi/\lambda)(p-\tilde{p})d_{Tx} + j2\pi\Delta t f_{T\max}\cos\gamma_T \\
&+ k_T\cos\mu_T, \\
&z_{DB1} = j(2\pi/\lambda)(q-\tilde{q})d_{Rx} + j2\pi\Delta t f_{R\max}\cos\gamma_R \\
&+ k_R\cos\mu_R, \\
&I_{T1} = \frac{2}{a^2}\left(e^{-jaR_{t2}}(1+jaR_{t2}) - e^{-jaR_{t1}}(1+jaR_{t1})\right), \\
&I_{R1} = \frac{2}{a^2}\left(e^{-jaR_{r2}}(1+jaR_{r2}) - e^{-jaR_{r1}}(1+jaR_{r1})\right), \\
&I_{SBT} = \frac{1}{2a^3}\Bigg[e^{-2jaR_{t2}}\Big(jc + 2ja^2R_{t2} + a - 2caR_{t2} \\
&- 2jca^2R_{t2}^2\Big) - e^{-2jaR_{t1}}\Big(jc + 2ja^2R_{t1} + a - 2caR_{t1} \\
&- 2jca^2R_{t1}^2\Big)\Bigg], \\
&I_{SBR} = \frac{1}{2a^3}\Bigg[e^{-2jaR_{r2}}\Big(jc + 2ja^2R_{r2} + a - 2caR_{r2} \\
&- 2jca^2R_{r2}^2\Big) - e^{-2jaR_{r1}}\Big(jc + 2ja^2R_{r1} + a - 2caR_{r1} \\
&- 2jca^2R_{r1}^2\Big)\Bigg], \\
&I_{T2} = \frac{1}{a^3}\Bigg[e^{-jaR_{t2}}\Big(2jc + ja^2R_{t2} + a - 2caR_{t2} \\
&- jca^2R_{t2}^2\Big) - e^{-jaR_{t1}}\Big(2jc + ja^2R_{t1} + a - 2caR_{t1} \\
&- jca^2R_{t1}^2\Big)\Bigg], \\
&I_{R2} = \frac{1}{a^3}\Bigg[e^{-jaR_{r2}}\Big(2jc + ja^2R_{r2} + a - 2caR_{r2} \\
&- jca^2R_{r2}^2\Big) - e^{-jaR_{r1}}\Big(2jc + ja^2R_{r1} + a - 2caR_{r1} \\
&- jca^2R_{r1}^2\Big)\Bigg]. \qquad (86)
\end{aligned}
$$

APPENDIX D
THE sD-PSDS OF THE SBT, SBR, DB, AND LoS COMPONENTS

The sD-psds of the single-bounced components can be obtained by noting that the functions $I_0\left(\sqrt{x_{SBT}^2 + y_{SBT}^2}\right)$ and $I_0\left(\sqrt{x_{SBR}^2 + y_{SBR}^2}\right)$ can be written as

$$
I_0\Bigg[j2\pi f_{T\max} \times \sqrt{t_T^2 + \left(\frac{p_{x_{SBT}}\sin\gamma_T}{f_{T\max}} - \frac{p_{y_{SBT}}\cos\gamma_T}{f_{T\max}} - \frac{w_{y_{SBT}}}{2\pi f_{T\max}}\right)^2}\Bigg], \qquad (87)
$$

$$
I_0\Bigg[j2\pi f_{R\max} \times \sqrt{t_R^2 + \left(\frac{p_{x_{SBR}}\sin\gamma_R}{f_{R\max}} - \frac{p_{y_{SBR}}\cos\gamma_R}{f_{R\max}} + \frac{w_{y_{SBR}}}{2\pi f_{R\max}}\right)^2}\Bigg], \qquad (88)
$$

where $t_T = \Delta t + A_{SBT}$ and $t_R = \Delta t + A_{SBR}$, and by using equality $\int_0^\infty J_0(\alpha\sqrt{t^2+u^2})\cos(\beta t)dt = \cos(u\sqrt{\alpha^2-\beta^2})/\sqrt{\alpha^2-\beta^2}$ [13, eq. 6.677-3]. Parameters in equations (87) and (88) are defined as follows:

$$
\begin{aligned}
A_{SBT} &= (2\pi p_{x_{SBT}}\cos\gamma_T + 2\pi p_{y_{SBT}}\sin\gamma_T - w_{x_{SBT}}) \\
&/\ 2\pi f_{T\max}, \\
p_{x_{SBT}} &= (p-\tilde{p})d_{Tx}/\lambda, \\
w_{x_{SBT}} &= jk_T\cos(\gamma_T - \mu_T), \\
p_{y_{SBT}} &= [(p-\tilde{p})d_{Ty} + (q-\tilde{q})d_{Ry}(R_{t1} \\
&+ 0.5(R_{t2}-R_{t1}))/D]/\lambda, \\
w_{y_{SBT}} &= jk_T\sin(\gamma_T - \mu_T), \\
A_{SBR} &= (2\pi p_{x_{SBR}}\cos\gamma_R + 2\pi p_{y_{SBR}}\sin\gamma_R + w_{x_{SBR}}) \\
&/\ 2\pi f_{R\max}, \\
p_{x_{SBR}} &= (q-\tilde{q})d_{Rx}/\lambda, \\
w_{x_{SBR}} &= -jk_R\cos(\gamma_R - \mu_R), \\
p_{y_{SBR}} &= [(q-\tilde{q})d_{Ry} + (p-\tilde{p})d_{Ty}(R_{r1} \\
&+ 0.5(R_{r2}-R_{r1}))/D]/\lambda, \\
w_{y_{SBR}} &= -jk_R\sin(\gamma_R - \mu_R). \qquad (89)
\end{aligned}
$$

After extensive calculations, the sD-psds of the SBT and the SBR components can be written as in (48), (49), respectively.

The first step in calculating the sD-psd of the DB component is to note that

$$
\begin{aligned}
&\mathcal{F}\left\{I_0\left(\sqrt{x_{DB}^2 + y_{DB}^2}\right) I_0\left(\sqrt{z_{DB}^2 + w_{DB}^2}\right)\right\} = \\
&\mathcal{F}\left\{I_0\left(\sqrt{x_{DB}^2 + y_{DB}^2}\right)\right\} \odot \mathcal{F}\left\{I_0\left(\sqrt{z_{DB}^2 + w_{DB}^2}\right)\right\} \qquad (90)
\end{aligned}
$$

where $\odot$ denotes convolution. Then, noting that the functions $I_0\left(\sqrt{x_{DB}^2 + y_{DB}^2}\right)$ and $I_0\left(\sqrt{z_{DB}^2 + w_{DB}^2}\right)$ can be written as

$$
I_0\Bigg[j2\pi f_{T\max} \times \sqrt{t_{DB1}^2 + \left(\frac{p_{x_{DB}}\sin\gamma_T}{f_{T\max}} - \frac{p_{y_{DB}}\cos\gamma_T}{f_{T\max}} + \frac{v_{y_{DB}}}{2\pi f_{T\max}}\right)^2}\Bigg], \qquad (91)
$$

$$
I_0\Bigg[j2\pi f_{R\max} \times \sqrt{t_{DB2}^2 + \left(\frac{p_{z_{DB}}\sin\gamma_R}{f_{R\max}} - \frac{p_{w_{DB}}\cos\gamma_R}{f_{R\max}} + \frac{v_{w_{DB}}}{2\pi f_{R\max}}\right)^2}\Bigg], \qquad (92)
$$

where $t_{DB1} = \Delta t + A_{DB1}$, $t_{DB2} = \Delta t + A_{DB2}$, and

$$
\begin{aligned}
A_{DB1} &= (2\pi p_{x_{DB}}\cos\gamma_T + 2\pi p_{y_{DB}}\sin\gamma_T + v_{x_{DB}}) \\
&/\ 2\pi f_{T\max}, \\
p_{x_{DB}} &= (p-\tilde{p})d_{Tx}/\lambda, \\
v_{x_{DB}} &= -jk_T\cos(\gamma_T - \mu_T), \\
p_{y_{DB}} &= (p-\tilde{p})d_{Ty}/\lambda, \\
v_{y_{DB}} &= -jk_T\sin(\gamma_T - \mu_T), \\
p_{z_{DB}} &= (q-\tilde{q})d_{Rx}/\lambda, \\
v_{z_{DB}} &= -jk_R\cos(\gamma_R - \mu_R), \\
p_{w_{DB}} &= (q-\tilde{q})d_{Ry}/\lambda,
\end{aligned}
$$

$$\begin{aligned} v_{w_{DB}} &= -jk_R \sin(\gamma_R - \mu_R), \\ A_{DB2} &= (2\pi p_{z_{DB}} \cos\gamma_R + 2\pi p_{w_{DB}} \sin\gamma_R + v_{z_{DB}}) \\ &/ \ 2\pi f_{R\max}, \end{aligned} \tag{93}$$

and using equality $\int_0^\infty J_0(\alpha\sqrt{t^2+u^2})\cos(\beta t)dt = \cos(u\sqrt{\alpha^2-\beta^2})/\sqrt{\alpha^2-\beta^2}$ [13, eq. 6.677-3], we obtain the sD-psd of the DB component in (50).

Finally, by calculating the Fourier transform of the STF-CF in (42), we obtain the sD-psd of the LoS component in (47).

APPENDIX E
THE PSDS OF THE SBT, SBR, DB, AND LOS COMPONENTS

We start the derivation for the psds of the SBT and SBR components by noting that the functions $I_0\left(\sqrt{x_{SBT}^2+y_{SBT}^2}\right)$ and $I_0\left(\sqrt{x_{SBR}^2+y_{SBR}^2}\right)$ can be written as

$$I_0\left(j\pi\frac{2R_t}{c_0}\sqrt{(\Delta f - B_{SBT})^2 + \left(\frac{C_{SBT}c_0}{2R_t\pi}\right)^2}\right), \tag{94}$$

$$I_0\left(j\pi\frac{2R_r}{c_0}\sqrt{(\Delta f - B_{SBR})^2 + \left(\frac{C_{SBR}c_0}{2R_r\pi}\right)^2}\right), \tag{95}$$

respectively, where

$$\begin{aligned} B_{SBT} &= (2\pi(p-\tilde{p})d_{Tx}/\lambda - jk_T\cos\mu_T)c_0/(2R_t\pi), \\ C_{SBT} &= (2\pi(p-\tilde{p})d_{Ty}/\lambda + 2\pi(q-\tilde{q})d_{Ry}(R_{t1} \\ &+ 0.5(R_{t2}-R_{t1})))/(D\lambda) - jk_T\sin\mu_T), \\ B_{SBR} &= (2\pi(q-\tilde{q})d_{Rx}/\lambda - jk_R\cos\mu_R)c_0/(2R_r\pi), \\ C_{SBR} &= (2\pi(q-\tilde{q})d_{Ry}/\lambda + 2\pi(q-\tilde{q})d_{Ty}(R_{r1} \\ &+ 0.5(R_{r2}-R_{r1})))/(D\lambda) - jk_R\sin\mu_R). \end{aligned} \tag{96}$$

Using the equality [13, eq. 6.677-3] and after extensive calculations, the psds of the single-bounced components can be written as in (52), (53), respectively.

Using (90), noting that the functions $I_0\left(\sqrt{x_{DB}^2+y_{DB}^2}\right)$ and $I_0\left(\sqrt{z_{DB}^2+w_{DB}^2}\right)$ can be written as

$$I_0\left(j\pi\frac{2R_t}{c_0}\sqrt{(\Delta f - B_{DB})^2 + \left(\frac{C_{DB}c_0}{2R_t\pi}\right)^2}\right), \tag{97}$$

$$I_0\left(j\pi\frac{2R_r}{c_0}\sqrt{(\Delta f - D_{DB})^2 + \left(\frac{E_{DB}c_0}{2R_r\pi}\right)^2}\right), \tag{98}$$

respectively, where

$$\begin{aligned} B_{DB} &= (2\pi(p-\tilde{p})d_{Tx}/\lambda - jk_T\cos\mu_T)c_0/(2R_t\pi), \\ C_{DB} &= 2\pi(p-\tilde{p})d_{Ty}/\lambda - jk_T\sin\mu_T, \\ D_{DB} &= (2\pi(q-\tilde{q})d_{Rx}/\lambda - jk_R\cos\mu_R)c_0/(2R_r\pi), \\ E_{DB} &= 2\pi(q-\tilde{q})d_{Ry}/\lambda - jk_R\sin\mu_R, \end{aligned} \tag{99}$$

and using the equality [13, eq. 6.677-3], we obtain the psds of the DB component in (54).

Finally, calculating the inverse Fourier transform of the STF-CF in (42), we obtain the psds of the LoS component in (51).

REFERENCES

[1] A. S. Akki and F. Haber, "A statistical model for mobile-to-mobile land communication channel," *IEEE Trans. Veh. Technol.*, vol. 35, pp. 2–10, Feb. 1986.

[2] A. S. Akki, "Statistical properties of mobile-to-mobile land communication channels," *IEEE Trans. Veh. Technol.*, vol. 43, pp. 826–831, Nov. 1994.

[3] R. Wang and D. Cox, "Channel modeling for ad hoc mobile wireless networks," in *Proc. IEEE VTC'02*, pp. 21–25, May 2002.

[4] C. S. Patel, G. L. Stüber, and T. G. Pratt, "Simulation of rayleigh-faded mobile-to-mobile communication channels," *IEEE Trans. Commun.*, vol. 53, pp. 1876–1884, Nov. 2005.

[5] A. G. Zajić and G. L. Stüber, "A new simulation model for mobile-to-mobile rayleigh fading channels," in *Proc. IEEE WCNC'06*, pp. 1266–1270, Apr. 2006.

[6] J. Maurer, T. Fügen, and W. Wiesbeck, "Narrow-band measurement and analysis of the inter-vehicle transmission channel at 5.2 GHz," in *Proc. IEEE VTC'02*, pp. 1274–1278, May 2002.

[7] G. Acosta, K. Tokuda, and M. A. Ingram, "Measured joint doppler-delay power profiles for vehicle-to-vehicle communications at 2.4 GHz," in *Proc. IEEE GLOBECOM'04*, pp. 3813–3817, Nov. 2004.

[8] G. Acosta and M. A. Ingram, "Model development for the wideband expressway vehicle-to-vehicle 2.4 GHz channel," in *Proc. IEEE WCNC'06*, pp. 1283–1288, Apr. 2006.

[9] M. Pätzold, B. O. Hogstad, N. Youssef, and D. Kim, "A MIMO mobile-to-mobile channel model: part one-the reference model," in *Proc. IEEE PIMRC'05*, pp. 573–578, Sept. 2005.

[10] A. G. Zajić and G. L. Stüber, "Space-time correlated mimo mobile-to-mobile channels," in *Proc. IEEE PIMRC'06*, Sept. 2006.

[11] B. O. Hogstad, M. Pätzold, N. Youssef, and D. Kim, "A MIMO mobile-to-mobile channel model: part two-the simulation model," in *Proc. IEEE PIMRC'05*, pp. 562–567, Sept. 2005.

[12] A. G. Zajić and G. L. Stüber, "Simulation models for mimo mobile-to-mobile channels," in *Proc. IEEE MILCOM'06*, Oct. 2006.

[13] I. S. Gradshteyn and I. M. Ryzhik, *Table of Integrals, Series, and Products* . San Diego, CA: A. Jeffrey, Academic, 5th ed., 1994.

[14] A. G. Zajić and G. L. Stüber, "Three-dimensional modeling, simulation, and capacity analysis of spacetime correlated mobile-to-mobile channels," *IEEE Trans. Veh. Technol.*, vol. 57, pp. 2042–2054, July 2008.

[15] A. G. Zajić, G. L. Stüber, T. G. Pratt, and S. Nguyen, "Wide-band MIMO mobile-to-mobile channels: geometry-based statistical modeling with experimental verification," *IEEE Trans. Veh. Technol.*, Mar. 2009. , to appear.

[16] A. G. Zajić, G. L. Stüber, T. G. Pratt, and S. Nguyen, "Envelope level crossing rate and average fade duration in mobile-to-mobile fading channels," in *Proc. IEEE ICC'08*, pp. 4446–4450, May 2008.

[17] D. Gesbert, H. Bölcskei, D. A. Gore, and A. J. Paulraj, "Outdoor mimo wireless channels: models and performance prediction," *IEEE Trans. Commun.*, vol. 50, pp. 1926–1934, Dec. 2002.

[18] G. L. Stüber, *Principles of Mobile Communication*. Kluwer, 2nd ed., 2001.

[19] A. Abdi, J. A. Barger, and M. Kaveh, "A parametric model for the distribution of the angle of arrival and the associated correlation function and power spectrum at the mobile station," *IEEE Trans. Veh. Technol.*, vol. 51, pp. 425–434, May 2002.

[20] J. D. Parsons and A. M. D. Turkmani, "Characterisation of mobile radio signals: model description," *IEE Proc. I, Commun., Speach, and Vision*, vol. 138, pp. 549–556, Dec. 1991.

[21] A. Kuchar, J. P. Rossi, and E. Bonek, "Directional macro-cell channel characterization from urban measurements," *IEEE Trans. Antennas Propag.*, vol. 48, pp. 137–146, Feb. 2000.

[22] P. Hoeher, "A statistical discrete-time model for the wssus multipath channel," *IEEE Trans. Veh. Technol.*, vol. 41, pp. 461–468, Nov. 1992.

[23] E. Chiavaccini and G. M. Vitetta, "Gqr models for multipath rayleigh fading channels," *IEEE J. Select. Areas Commun.*, vol. 19, pp. 1009–1018, June 2001.

[24] R. S. Kennedy, *Fading Dispersive Communication Channels*. New York: Wiley-Interscience, 1969.

[25] Z. Latinovic, A. Abdi, and Y. Bar-Ness, "On the utility of the circular ring model for wideband MIMO channels," in *Proc. IEEE VTC'04*, pp. 96–100, Sept. 2004.

[26] K. V. Mardia and E. P. Jupp, *Directional Statistics*. New York: Wiley, 1999.

Alenka G. Zajić (S'99-M'08) received the B.Sc. and M.Sc. degrees form the School of Electrical Engineering, University of Belgrade, in 2001 and 2003, respectively. She received her Ph.D. degree in Electrical and Computer Engineering form the Georgia Institute of Technology in 2008. From 2001 to 2003, she was a design engineer for Skyworks Solutions Inc., Fremont, CA. Currently, she is the president of AlZaComm, Atlanta. Her research interests are in wireless communications and applied electromagnetics.

Dr. Zajić received the Best Paper Award at ICT 2008, the Best Student Paper Award at WCNC 2007, and was also the recipient of the Dan Noble Fellowship in 2004, awarded by Motorola Inc. and IEEE Vehicular Technology Society for quality impact in the area of vehicular technology.

Gordon L. Stüber (S'81-M'82-SM'96-F'99) received the B.A.Sc. and Ph.D. degrees in Electrical Engineering from the University of Waterloo, Ontario, Canada, in 1982 and 1986 respectively. In 1986, he joined the School of Electrical and Computer Engineering, Georgia Institute of Technology, where is the Joseph M. Pettit Chair Professor.

Dr. Stüber was co-recipient of the IEEE Vehicular Technology Society Jack Neubauer Memorial Award in 1997 for the best systems paper. He became an IEEE Fellow in 1999 for contributions to mobile radio and spread spectrum communications. He received the IEEE Vehicular Technology Society James R. Evans Avant Garde Award in 2003 for contributions to theoretical research in wireless communications.

Dr. Stüber served as General Chair and Program Chair for several conferences, including VTC'96, ICC'98, MMT"00, CTW'02, and WPMC'02. He is a past Editor for IEEE TRANSACTIONS ON COMMUNICATIONS (1993-1998), and served on the IEEE Communications Society Awards Committee (1999-2002). He an elected member of the IEEE Vehicular Technology Society Board of Governors (2001-2003, 2004-2006) and received the Outstanding Service Award from the IEEE Vehicular Technology Society.